Life-cycle fragility analysis of aging reinforced concrete bridges

A dynamic Bayesian network approach

Molaioni, Filippo; Andriotis, Charalampos P.; Rinaldi, Zila

DOI
10.1016/j.strusafe.2025.102654

Publication date
2026

Document Version
Final published version

Published in
Structural Safety

Structural Safety 119 (2026) 102654

Contents lists available at ScienceDirect

Structural Safety

journal homepage: www.elsevier.com/locate/strusafe

Life-cycle fragility analysis of aging reinforced concrete bridges: A dynamic Bayesian network approach

Filippo Molaioni [a,*], Charalampos P. Andriotis [b,*], Zila Rinaldi [a]

[a] Department of Civil Engineering and Computer Science Engineering, University of Rome Tor Vergata, via del Politecnico 1, 00133 Rome, Italy
[b] Faculty of Architecture and the Build Environment, Delft University of Technology, 2628 BL Delft, the Netherlands

ARTICLE INFO

Keywords:
Dynamic Bayesian Networks
Seismic fragility analysis
Aging bridges
Life-cycle risk assessment
Chloride corrosion
Concrete structures

ABSTRACT

Reinforced concrete bridges are predominant structural systems in transportation infrastructure. Their exposure to chronic and sudden stressors, such as corrosion and earthquakes, make them prone to risks with severe socioeconomic consequences. While time-dependent single-component seismic fragility formulations have advanced the frontier of life-cycle probabilistic risk assessment, state-dependent multi-component representations of damage and deterioration, paramount for structural integrity management, still lack a systematic probabilistic framework. This paper develops a novel dynamic Bayesian network to evaluate the life-cycle fragility functions of aging bridges, encapsulating the impacts of corrosion and seismic phenomena over time. The network establishes Markovian transitions among deterioration states for various bridge components integrating chloride diffusion and corrosion propagation models with non-stationary Gamma processes. A methodology for deriving and state-dependent fragility at the component and system levels depending on several deterioration scenarios is presented. Our framework is exemplified in an archetypical 4-span bridge, demonstrating the longitudinal effects of corrosion on the system's seismic fragility for splash and atmospheric conditions. Insights from the multi-component analysis highlight the capabilities in understanding the pathologies and evolving mechanical interactions among components. The adaptability in accommodating on-site observations and advanced decision-making algorithms is discussed, demonstrating the suitability of the framework for applications requiring flexible and updatable virtual environments.

1. Introduction

Bridges, critical components of transportation infrastructure, need to endure a spectrum of continuous and sudden stresses during their life-cycle. Assessing long-term safety and resilience, particularly for those built with reinforced concrete (RC), is a complex task due to the multifaceted uncertainties that characterize material properties, detailing, and deterioration. Among many factors, the combined effect of corrosion of steel rebars and seismic actions poses a major threat that can result in catastrophic failures and network disruptions with significant reconstruction costs. Over the past decades, there has been growing interest in assessing the lifespan and resilience of these structures. Early studies by [59] and [65] have identified the role of several factors in degradation mechanisms, such as the adverse effects of deicing salts, and the importance of concrete cover thickness and compressive strength. It is also well understood that steel corrosion phenomena in reinforced concrete intensify over time, exacerbating significantly structural vulnerabilities. It macroscopically progresses in two stages: (i) initiation, defined by the penetration of the concrete cover by aggressive agents (i.e., carbon dioxide, chlorides) and (ii) propagation, defined by the active loss of steel mass due to the corrosion reaction [6,60]. Several experimental campaigns have been carried out in the last decades to explore the structural impact of corrosion further, thus revealing the reducing effects on mechanical properties of steel rebars, concrete cover and bond strength, which result in bearing capacity reductions, increases in deflection, and growth of crack widths [10–11,15,26,51]. In particular, [26] shed light on how corrosion degrades the mechanical properties of rebars and defined a degradation law for both uniform and pitting corroded rebars based on experimental tensile tests. Other experimental studies showed that corrosion dramatically reduces structural ductility, strength, strain capacity, and seismic performance of RC columns and coastal bridge piers, particularly in seismic-prone areas [34,50,68]. More recent research by [19] and [18] underscored that corrosion can alter the structural

* Corresponding authors.
E-mail addresses: filippo.molaioni@students.uniroma2.eu (F. Molaioni), C.Andriotis@tudelft.nl (C.P. Andriotis).

https://doi.org/10.1016/j.strusafe.2025.102654
Received 18 February 2025; Received in revised form 3 June 2025; Accepted 10 September 2025
Available online 15 September 2025

performance of RC and prestressed concrete beams and Gerber half-joints by changing their failure mechanism, emphasizing the importance of accurately accounting for behavior modifications due to corrosion in structural assessments. Besides strength and ductility reduction for the main concrete members, corrosion also affects the performance of smaller, yet critical, bridge compartments, such as steel bearings [30,56]. In [30], an extensive experimental program on the cyclic behavior of several steel bearing specimens from existing reinforced concrete bridges is set up, providing analytical formulations for the ultimate strength of bearings and modeling guidelines for their cyclic behavior.

On top of deterioration, extreme event hazards, such as those manifested in seismic-prone regions, play a crucial role in life-cycle structural reliability of bridges. Past earthquakes have shown common forms of seismic damage to bridges, including unseating of the deck due to bearings failure, column failures, and pounding between deck elements as shown, for example, in Fig. 1 [1,48,49,64,66].

Therefore, understanding and mitigating bridge structural and durability weaknesses is necessary to prevent catastrophic failures during earthquakes. Bridges are heterogeneous time-dependent systems, where local component dynamics interact to eventually define global systemic behaviors and risks over the entire life-cycle. Numerous studies have dealt with the quantification of safety losses for deteriorating RC structures and bridges [2,7–8,9,12,14,17,23–24,28,41,45,53,54]. Among these, [41] presented a methodology for generating seismic fragility curves for highway bridges that considers multiple major components (i.e., columns, bearings, and abutments). Even though the deterioration phenomena were not included, the authors emphasized the importance of a multi-component system perspective for comprehensive assessment of losses. In the context of multi-component approaches, an efficient framework was developed and refined in [23–24,53,54]. This allows for the seismic fragility and cost analysis of RC bridges by modeling the deterioration phenomena for both bearing and column components. The methodology emphasizes the role of environmental exposure conditions and multiple deterioration mechanisms, specifically accounting for pitting corrosion in steel rebars and necking effects in bearing anchor bolts.

Such probabilistic frameworks allow for effective risk predictions by assessing both deterioration and seismic safety of bridges and their components at given time-points within the life-cycle. However, decision-making for these structures can become more precise if we are able to account for combinations of deterioration and damage, i.e. by developing joint state-based and time-based approaches. This also gives a decision-maker the opportunity to update structural deterioration or fragility states based on monitoring and inspection information. An updatable virtual simulation environment for longitudinal seismic performance can further cater to needs of state-of-the-art algorithmic decision-making, an advancement that is instrumental for efficiently maintaining the massive stock of aging concrete bridges. In recent years, the field of decision-making under uncertainty for existing structures has focused on coupling stochastic deterioration models, Bayesian decision principles, and stochastic optimal control algorithmic procedures [3,4,27,44,46]. Given the complexity of inspection and maintenance planning, featuring numerous possible actions in highly probabilistic environments, the problem has been shown to be efficiently defined within the global optimization framework of partially observable Markov decision processes. This allows us to obtain comprehensive state-based policies for structural interventions. [3,4] introduced deep reinforcement learning to determine such optimal policies in large state and action spaces, showcasing the significant suboptimality resulting from existing time- and condition-based maintenance methods in handling multi-component systems with complex decision-making requirements. At the core of the formulation is expressing the deteriorating environment as a dynamic Bayesian network (DBN), which allows for efficient state uncertainty propagation and data-driven inference over multiple time steps. A number of recent studies demonstrate the efficacy of DBNs for optimal inspection and maintenance, such as [25,29,39]. Among these, [38] addresses the computational complexity of large correlated state spaces, proposing an algorithmic framework for managing deteriorating offshore wind turbines combining Bayesian networks and deep reinforcement learning.

The value of state-dependent fragility functions for representing seismic vulnerability conditioned on a structure's evolving state has been also recently demonstrated. Examples include energy-based approaches for mainshock–aftershock sequences [22,47], vibration-based frameworks for sequential damage assessment of bridges [5], as well as extended and generalized formulations [3]. More recent applications range from simplified predictive models for multi-story moment-resisting frame structures [42] to uncertainty-quantification frameworks for industrial components [40]. While these studies confirm the importance

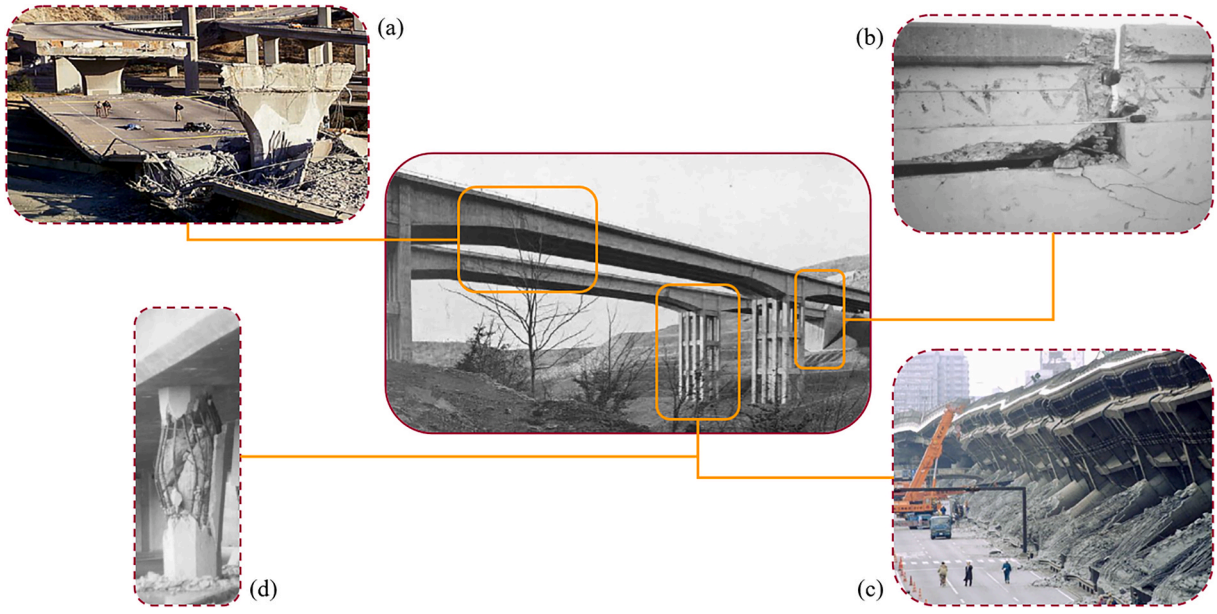

Fig. 1. Typical damages in the bridge structural components during an earthquake. a) Deck unseating and bearings failure (Northridge 1994); b) Pounding between deck's components (Northridge 1994); c) Columns failure (Kobe 1995); d) Column failure (San Fernando 1971).

of conditioning fragility on discrete states, none of them couples corrosion deterioration states of multiple components to the seismic response of bridges. The present work extrends this research field by quantifying discrete corrosion states for several bridge components and using them as the basis for state-dependent seismic fragility functions.

Addressing the need for complex state- and time-based virtual environments, this paper proposes a DBN framework for the life-cycle seismic safety assessment of aging bridges. The framework develops and integrates transition matrices for the corrosion deterioration dynamics of structural components and updatable, time-invariant, state-dependent seismic fragility functions conditioned on them for both structural components and the system. This provides a dynamic multi-component representation of the long-term effects of corrosion and seismic activity on bridges, thereby enabling both comprehensive risk quantification and seamless integration with decision-making algorithms.

In Section 2, the DBN approach is described, and corrosion deterioration states (CDSs) and seismic damage states (SDSs) are defined to encapsulate the problem in a discrete space. This section also details the process of calculating transition matrices among CDSs and the methodology to link these to SDSs by calculating state-dependent fragility functions. Furthermore, the modeling methodologies for the nonlinear behavior of bridge components, including corrosion effects, are described in the same section. The method is applied to a case-study bridge, which is described in Section 3. The structure is modeled as a multi-component system, consisting of columns and several bearing components types. Results are presented in Section 4 and include: non-stationary transition matrices for CDSs of components for two extreme environmental conditions, namely atmospheric and splash ones; state-dependent fragility curves for structural components and the system according to various SDSs and corrosion scenarios (i.e., combinations of CDSs for components); and the longitudinal effects of corrosion on seismic fragility of the system in time. Finally, a discussion is provided in Section 5, concerning the main findings and future capabilities enabled by the proposed formulation, including: the capability of the approach to capture the sensitivity of the case-study bridge's seismic safety to corrosion; the method's potential in identifying the most vulnerable components and informing retrofit solutions; its extendability in integrating on-site observations and being integrated with AI-driven algorithmic decision-making.

2. Methodology

2.1. DBN for life-cycle seismic fragility of deteriorating bridges

Seismic fragility functions represent the probability of a structure exceeding a seismic damage state (SDS). It maps structural damage to a discrete SDS space, based on an engineering demand parameter (EDP), given an intensity measure (IM) of the seismic action. Considering aging reinforced concrete bridges, the seismic fragility is expected to increase over time due to structural deterioration; therefore, its quantification requires, in general, the use of a large number of analyses that must combine the effects of corrosion and multiple seismic events over the structural lifetime. To efficiently address this problem, we develop a dynamic Bayesian network (DBN) for quantifying the risk of aging bridges over their life-cycle as shown in Fig. 2.

A DBN is a directed acyclic graphical model that is particularly suitable for modeling temporal deterioration and its accompanying uncertainties and can be readily combined with real-time data for state inference and model updating. In such a model, variables are introduced through nodes, while directed links represent conditional probabilities between these. This way, it is possible to decompose the entire problem into smaller, easier-to-compute components by evaluating each probabilistic dependency with independent analyses. To gain insight into the operation of the DBN, the modeling assumptions for the bridge structural system must be identified. In order to consider the various mechanisms that characterize the typical seismic damage levels in bridges, the aging bridge structure is thus idealized as a multi-component system.

The components considered in this study are those that play a crucial role in the seismic response of the structure, since they can control the system's nonlinear behavior and are highly prone to deterioration phenomena. Specifically, these are the columns (COL), and the steel bearings (BEA), among which we considered the high type fixed bearings (HTFB), the high type expansion bearings (HTEB), and the low type fixed bearings (LTFB). Generally, the parameters that describe the deterioration of these components are continuous. However, to infer life-cycle fragility using dynamic Bayesian networks we also express deterioration in a discrete state space through the vector of the CDSs of the system components. Furthermore, the components are classified according to two typologies: COL (i.e., columns only), and BEA (i.e., HTFB, HTEB, LTFB). Assuming that components belonging to a single category share the same CDS, the state space of the corrosion scenarios (i.e., combination of CDSs for components) is reduced. Following this approach, it is possible to define the system/components fragility over its/their life-cycle, representing the probability of exceeding a given SDS, given the vector of IMs of the seismic action, the CDSs of the components and the SDS reached up to the previous time-step:

$$P_{SDS,t} = P(SDS_t \geq s \,|IM_{0:t},\, CDS_{0:t},\, SDS_{0:t-1}) \tag{1}$$

This study uses the peak ground acceleration (PGA) for the IM of the seismic ground motion. However, alternative intensity measures can also be employed [55], including peak ground velocity, spectral acceleration, average spectral acceleration, spectral intensity and modified Mercalli intensity.

SDSs for structural components are defined as "Intact", "Slight", "Moderate", "Extensive" and "Complete". These limit states have been qualitatively defined by [21]. Specifically:

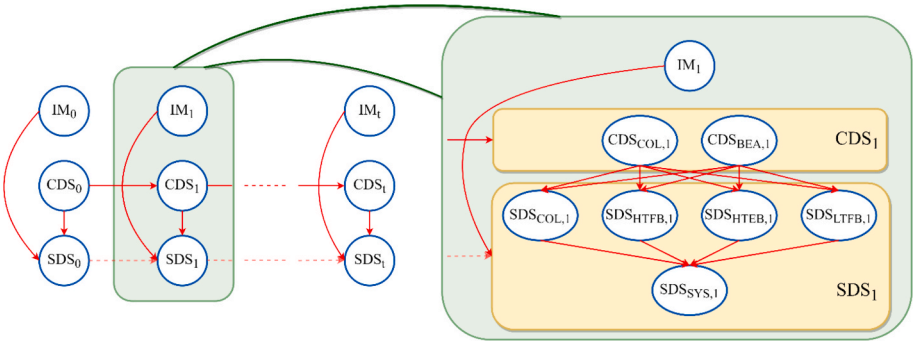

Fig. 2. DBN for life-cycle seismic fragility of deteriorating bridges. The overall model including nodes and transitions (left) and interactions among component and system states within a single time step (right). COL = columns; HTFB = high type fixed bearings; HTEB = high type expansion bearings; LTFB = low type fixed bearings; SYS = system.

- No detectable cracks or other damage define the “Intact” state;
- Minor cracks and spalling of the concrete correspond to the “Slight” state;
- Moderate cracks and spalling of concrete and failures in the bearings without any unseating of the deck define the “Moderate” state;
- Structurally unsafe columns due to severe damage or bearings with significant residual displacement and settlements define the “Extensive” state;
- Any column collapse or loss of bearing support leads to the “Complete” state.

In [41], quantitative thresholds for those limit states, related to reinforced concrete bridges, are derived through Bayesian updating by combining physics-based prescriptive [13], and judgement-based descriptive [43], definitions of the aforementioned limit states. These quantitative thresholds are adopted in Table 1 and employed in the proposed approach to describe the SDSs of the bridge components.

The discretization in CDSs is part of the design assumption for the DBN and is informed by existing literature. In this study, the CDSs are classified as: “0: Sound”, “1: Initial”, “2: Progressive”, and “3: Critical”. Each state is qualitatively described as follows:

- The “Sound” state indicates that corrosion phenomena have not yet begun. Aggressive environmental agents, such as carbon dioxide and chlorides, may be present in the concrete, but their depth or contents are insufficient to initiate corrosion.
- The “Initial” state corresponds to a slight-to-medium corrosion intensity of the structural components. Cracks may appear locally on the concrete surface, and the structural capacity is expected to decrease relatively proportionally with the increase in the rebars’ average mass loss, since no substantial changes in the failure mechanism are expected at this stage.
- The “Progressive” state denotes medium-to-high corrosion intensity. Concrete component surfaces are affected by significant spalling, and the extension of corrosion affects many structural elements. The structural behavior may change substantially due to deterioration, even non-linearly, potentially leading to changes in the failure mechanisms.
- The “Critical” state signifies extreme corrosion intensity. The structural components are critically corroded, both locally and globally. Severe deterioration of linear and nonlinear structural performance is anticipated at this stage.

The corrosion intensity parameters that define these states include the mass loss of rebars and bolts (M_{loss} [%]) for columns and bearings, respectively; the steel plates thickness reduction (PTR [mm]) for bearings; and the additional coefficient of friction (k_{corr} [-]) for expansion bearings, which accounts for the interlocking effects due to corrosion. The specific discretization and value ranges of these quantities assumed in this study are provided in Table 2 for each component typology, i.e., the column component (CDS_{COL}) and the bearings component (CDS_{BEA}). Further details about the deterioration phenomena affecting the bridge components, the parameters describing the corrosion intensity, and the mechanical effects on the cyclic behavior of components are provided in Section 2.3.

To complete the description of the probabilistic graphical model, the following conditional probabilities between variables are introduced: (i) $f_{CDS=j}(i,t)$, the Markovian transition that describes the probability of having a corrosion state CDS $= j$ at time $t+1$, given corrosion state CDS $= i$ at the previous time step t; and (ii) $f_{SDS>s}(x,i,s')$, the state-dependent and time-invariant fragility functions, describing the probability of the bridge exceeding a seismic damage state SDS, given the IM vector, and the corrosion deterioration state CDS:

$$f_{CDS=j}(i,t) = P(CDS_{t+1} = j \,|\, CDS_t = i) \tag{2}$$

$$f_{SDS>s}(x,\, i,\, s') = P(SDS_t > s \,|\, IM_t = x,\, CDS_t = i, SDS_{t-1} = s') \tag{3}$$

Furthermore, a Markovian transition between SDS nodes over time helps consider that the resulting structural damage carries over to the next time step if no repair action is taken. Therefore, the time-dependent nature of the seismic risk for aging structures is dynamically described through time-slices connected by conditional probabilities among CDS nodes, for which the Markovian assumption is considered. This way, CDS at time step $t+1$ depends only on the CDS in slice t:

$$P(CDS_t) = P_0(CDS) \prod_{\tau=0}^{t-1} P(CDS_{\tau+1} | CDS_\tau) \tag{4}$$

It is worth noting that, as CDSs are discrete, and the corrosion phenomenon is time-dependent, Markovian transitions are described by a non-stationary matrix. The methodology for determining these transitions is described in detail in Section 2.2, while implementation with respect to a specific case study is reported in Section 4. Seismic events are considered to be independent, thus IM variables are covariates of state variables that do not depend on each other temporally, therefore, they are not subject to discretization. Seismic fragility functions are consequently represented by continuous functions. The methodology for determining these transitions is described in Section 2.3, while results related to our case study are reported in Section 4. In conclusion, it is crucial to underscore that, as depicted in Fig. 2, the variables IM_t, CDS_t, and SDS_t are represented as vectors. This is because each one encompasses data across various bridge component typologies, such as columns and bearings, reflecting the fact that a bridge comprises multiple columns and bearing devices. Thus, these vectors facilitate a comprehensive modeling of seismic fragility and deterioration for each individual component within the overall structural system.

2.2. Non-stationary transition for corrosion initiation and propagation

Non-stationary transitions among CDSs are computed via

Table 2
Corrosion deterioration states.

CDS		0: Sound	1: Initial	2: Progressive	3: Critical
Component	**Parameter**	**LB-UB**	**LB-UB**	**LB-UB**	**LB-UB**
COL	M_{loss} [%]	0–0	0–15	15–30	30–45
BEA	M_{loss} [%]	0–0	0–15	15–30	30–45
BEA	PTR [mm]	0–0	0–3.5	3.5–5.1	5.1–6.5
BEA	k_{corr} [-]	0–0	0–0.35	0.35–0.64	0.64–0.92

*M_{loss} = rebar/bolt mass loss [%], PTR = plate thickness reduction [mm], k_{corr} = additive coefficient of friction for expansion bearings [-].

Table 1
Probabilistic seismic damage states thresholds.

Component	EDP	Slight		Moderate		Extensive		Complete	
		M	**D**	**M**	**D**	**M**	**D**	**M**	**D**
COL	Curvature ductility [-]	1.29	0.59	2.1	0.51	3.52	0.64	5.24	0.65
BEA — Expansion	Displacement [mm]	37.4	0.6	104.2	0.55	136.1	0.59	187	0.65
BEA — Fixed	Displacement [mm]	6	0.25	20	0.25	40	0.47	187	0.65

*M = median of the lognormal distribution, D = Dispersion of the lognormal distribution.

probabilistic forward simulation of the deterioration phenomenon over the bridge lifespan. The flowchart outlining the framework developed to address this task is presented in Fig. 3.

Corrosion states are defined by the ranges reported in Table 2. The corrosion intensity parameter determining the transition from one state to another over the life-cycle is the mass loss of rebars and bolts (M_{loss} [%]), for column and bearing components, respectively. Other corrosion parameters, i.e., PTR [mm] and k_{corr}, are assumed to follow the same transitions. Moreover, in accordance with the proposed DBN, the structural lifespan is discretized into yearly time-steps. Transitions among states are thus evaluated through a probabilistic and iterative process, evaluating for each sample the yearly increase in the corrosion intensity parameter defining any CDS change at time $t+1$, starting with an initial guess of CDS at time t. For this, two deterioration models are considered, accounting for the two stages of the phenomenon, i.e., initiation and propagation. This two-stage approach, when combined with uncertainty propagation within a probabilistic assessment, enables the calculation of yearly state transitions. In particular, in the first model, namely the "Initiation Model" (Fig. 3, red box), uncertainties in environmental conditions, material and geometry (details are given in Section 3) are propagated through Monte Carlo simulation in order to obtain statistics on the time of corrosion initiation, T_{corr}, and to determine the transition probability of corrosion activation (i.e., CDS $\neq 0$) at any time step t. The second model, namely the "Propagation Model" (Fig. 3, blue box), allows the calculation of the yearly corrosion rate and, therefore, any change in the CDS based on the corrosion features (i.e., M_{loss} [%] as intensity, pitting factor R as morphology indicator, and the T_{corr} which affects the corrosion rate over time) through a second Monte Carlo simulation. This process is iterated on every time step t and for any $CDS_t = i$, thus determining the number of samples that, from a given CDS $= i$ at time t, transition to a CDS $= j$ at time $t+1$. Therefore, the non-stationary transition model, is estimated at any iteration as:

$$f_{CDS=j}(i,t) = P(CDS_{t+1} = j \,|CDS_t = i) = \frac{\sum_{samples}(CDS_{t+1} = j \cap CDS_t = i)}{\sum_{samples}(CDS_t = i)} \tag{5}$$

The initiation model resumed by the blue box in the flow-chart of Fig. 3 is further elucidated. Chloride corrosion occurs when the chloride content at the depth of the bars, C, exceeds the critical threshold, C_{cr}, thus destroying the protective film of the reinforcing rebars, exposing them to aggressive agents. Fick's second law captures chloride penetration into the concrete:

$$\frac{\partial C(x,t)}{\partial t} = -\frac{D_c \partial^2 C(x,t)}{\partial x^2} \tag{6}$$

A common assumption made in predictive models for corrosion initiation to solve Eq. (6) is that of constant chloride content at the outer surface C_s [12,14,23,53], leading to the following solutions for calculating chloride content at bar depth:

$$C(x,t) = \chi C_s \left[1 - \mathrm{erf}\left(\frac{x}{2\sqrt{D_c t}}\right)\right] \tag{7}$$

where C_s is the equilibrium chloride concentration at the concrete surface, erf is the Gaussian error function, x is the distance from the concrete surface corresponding to a chloride concentration in the concrete equal to C(x,t), and t the time in years, as proposed in [52]. D_c the diffusion coefficient computed as:

$$D_c(t) = D_0 \left(\frac{t_0}{t}\right)^a e^{b_e\left(\frac{1}{T_{ref}} - \frac{1}{T_{real}}\right)} \tag{8}$$

where D_0 is the initial diffusion coefficient, t_0 is set equal to 28 days, a is an aging exponent accounting for the decrease of D_c with time, b_e is a regression variable, T_{ref} is set equal to 253.15° K and T_{real} is the mean annual temperature [36,37].

The time to corrosion initiation, T_{corr} [years], which defines the transition from CDS $= 0$ to CDS $\neq 0$, is thus determined by discretizing the structural lifetime in yearly time-slices and determining the first slice when $C(x,t) > C_{cr}$. Thus, it is possible to calculate the probability of corrosion activation by modifying (5) as:

$$P(CDS_{t+1} \neq 0 | CDS_t = 0) = \frac{\sum_{samples}(T_{corr} = t+1)}{\sum_{samples}(T_{corr} \leq t)} = \frac{F_{T_{corr}}(t+1) - F_{T_{corr}}(t)}{(1 - F_{T_{corr}}(t))} \tag{9}$$

where F_{Tcorr} represents the cumulative density function for random variable T_{corr} estimated assuming a lognormal distribution [12]. To obtain the transition from CDS $= 0$ to others, the probability of corrosion activation, calculated in Eq. (9), is combined with the propagation model to calculate the yearly increase in corrosion, as explained in the next paragraph. It is worth highlighting that assuming T_{corr} as a random variable lognormally distributed also allows for the calculation of the corrosion rate in the propagation phase and, therefore, for the transition probability. Details on the random variables adopted in this study for the Monte Carlo simulations are given in Section 3.

The corrosion propagation model is used for determining CDSs transitions of structural components over time. In this framework, the mean annual increase in uniform bar penetration is determined based on the propagation model proposed by [65], and considering a CoV of 0.5 as suggested in [52]. This propagation model is used to calculate the time-dependent annual mean current intensity $i_{corr}(t)$, (10), and the mean uniform corrosion penetration increase $\lambda_m(t)$, which is directly linked to the current density through Faraday's law, as illustrated in Eq. (11):

$$i_{corr}(t) = 0.85 * \frac{37.5\left(1 - \frac{w}{c}\right)^{-1.64}}{xc} (t - T_{corr})^{0.29} \tag{10}$$

$$\lambda_m(t) = 0.0116 * i_{corr}(t) \tag{11}$$

where w/c is the concrete water-cement ratio; x_c is the concrete cover depth; and T_{corr} is the time of corrosion initiation.

It is worth noting that the magnitude of current density diminishes over time because the oxide production forms a protective layer over the bar, inhibiting the diffusion of iron ions. As such, transitions are non-stationary and their evaluation must be made for each time-step. Moreover, the calculation of the current density in Eq. (11) requires the time of corrosion initiation, T_{corr} [years], consequently, the statistics derived from the corrosion initiation model are used to account for its variability by sampling a value of T_{corr} accordingly.

Over time, the phenomenon is influenced by environmental factors and concrete parameters, and it is strongly characterized by aleatoric uncertainties. To encapsulate this randomness, the annual increase of corrosion penetration in steel rebars, $\lambda(t)$, is modeled through a Gamma process, characterized by a probability density function $Ga(\lambda(t))$ delineated in Eq. (12), whose shape α and rate β factor are defined in Eq. (13), following the approach proposed by [3]:

$$Ga(\lambda(t)) = \frac{\beta^\alpha}{\Gamma(\alpha)} \lambda(t)^{\alpha-1} e^{\beta\lambda(t)} \tag{12}$$

$$\alpha = \left(\frac{\lambda_m(t)}{\sigma}\right)^2; \; \beta = \frac{\lambda_m(t)}{\sigma^2} \tag{13}$$

Transitions between CDSs are determined by calculating the annual increase in rebar and bolt mass losses. To this end, a corrosion morphology model must be introduced to appropriately convert the mean annual penetration into a mean annual mass loss. In this study, the model proposed by [61], described in Fig. 4, is adopted. This relates the maximum penetration p in the rebar and the mass loss trough Eqs. (14)-

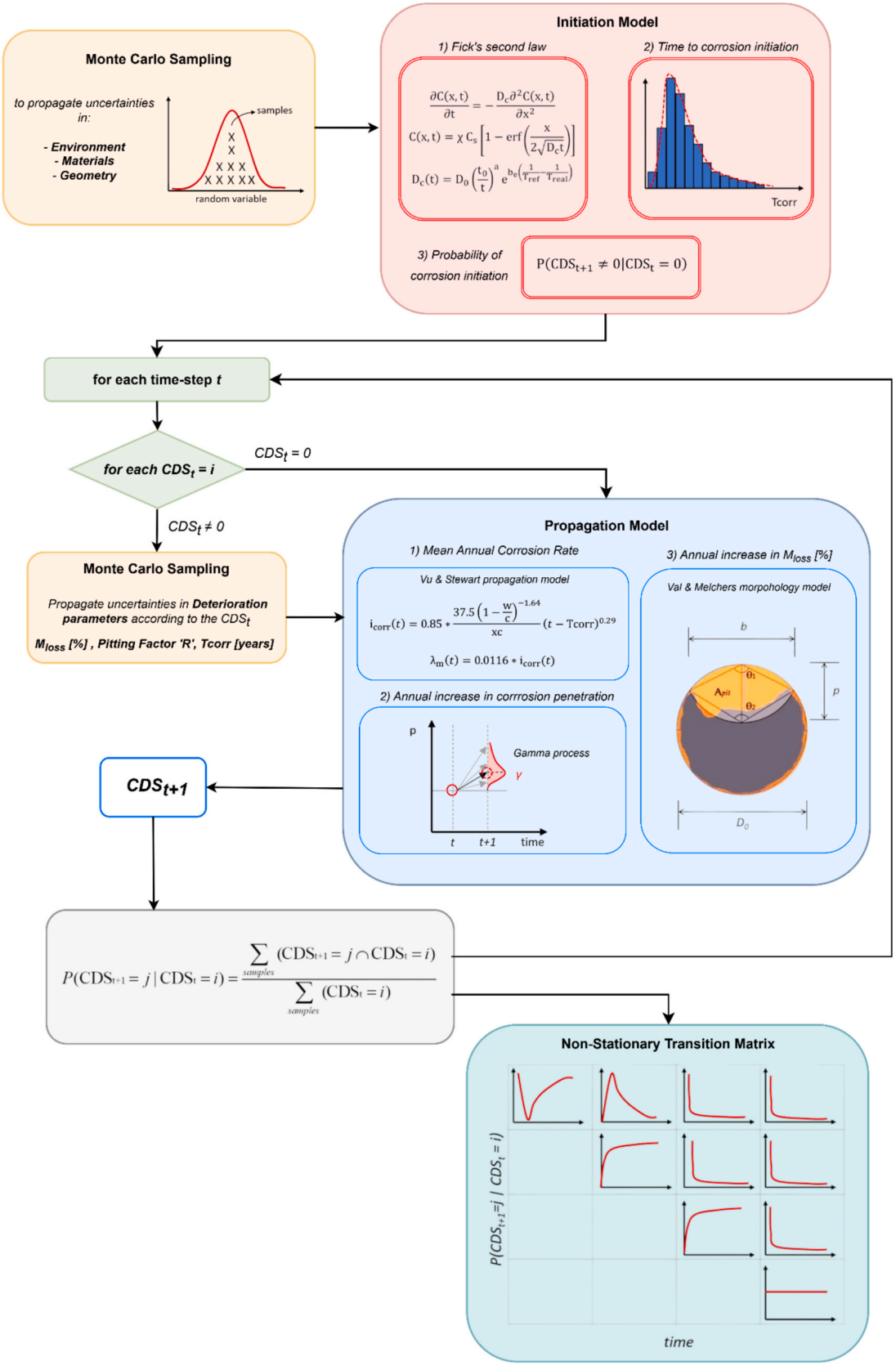

Fig. 3. Flowchart for the proposed methodology to compute the non-stationary transitions.

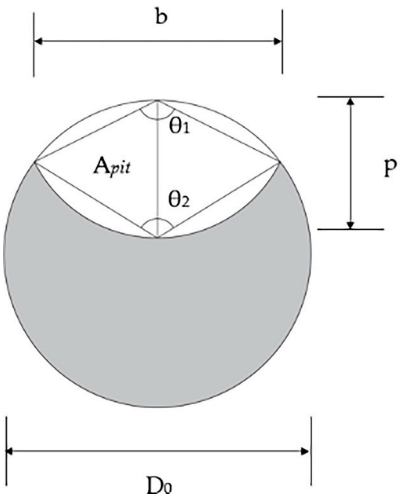

Fig. 4. Morphology model by [61].

(16).

$$\begin{cases} A_{pit} = A_1 + A_2 & if\ p \le \dfrac{D_0}{\sqrt{2}} \\ A_{pit} = A_0 - A_1 + A_2 & if\ \dfrac{D_0}{\sqrt{2}} \le p \le D_0 \\ A_{pit} = A_0 & if\ p \ge D_0 \end{cases} \tag{14}$$

$$A_1 = 0.5^*\left[\theta_1\left(\frac{D_0}{2}\right)^2 - b\left|\frac{D_0}{2} - \frac{p^2}{D_0}\right|\right]$$

$$A_2 = 0.5^*\left[\theta_2 p^2 - b\frac{p^2}{D_0}\right], A_0 = \frac{\pi^* D_0^2}{4} \tag{15}$$

$$b = 2^*p^*\sqrt{1-\left(\frac{p}{D_0}\right)^2}, \theta_1 = 2^*\arcsin\left(\frac{b}{D_0}\right),$$

$$\theta_2 = 2^*\arcsin\left(\frac{b}{2^*p}\right) \tag{16}$$

where D_0 refers to the original diameter of the rebar; A_{pit} represents the cross-sectional area of the pit; A_0 is the cross-sectional area of the sound rebar; p refers to the radius of the pit penetration; while θ_1, θ_2, A_1, A_2 and b are pit geometrical parameters.

The adopted morphological model is integrated with the propagation model, establishing a relationship between the annual increase in maximum penetration and the average percentage increase in the mass loss, M_{loss} [%]. To incorporate uncertainties associated with corrosion morphology, a value of the pitting factor, R, which is defined as the ratio between the maximum and the uniform penetration, is sampled considering it as a random variable, following a Gumbel distribution, as proposed by [58].

In our iterative probabilistic approach of Fig. 3, the propagation model is employed to determine the state transitions of CDSs for each sample and each time step. It is crucial to note that the propagation model requires, for each sample, an initiation time value T_{corr} [years], a pitting factor value R [-], and a mass loss M_{loss} [%] associated with the CDS at time *t*. At this stage, the T_{corr} [years] value is sampled from a lognormal distribution [12], whose parameters are based on the results of the initiation model. The R [-] value is sampled considering a Gumbel distribution, adopting the parameters proposed in [58]. The M_{loss} [%] value is selected in accordance with the CDS at time *t*, considering uniform distributions based on the ranges provided in Table 2. Therefore, for each time interval, we sample these values for a total 10^6 samples. This procedure allows us to calculate the annual increase in M_{loss} [%] and, consequently, the CDS at time $t+1$ for each sample. By analyzing the set of samples, we evaluate the annual transition probability for each pair of states CDS_t and CDS_{t+1}, using Eq. (5).

2.3. State-dependent fragility curves

Estimating state-dependent and time-invariant fragility functions involves the comparison of probabilistic demand parameters and capacity limit states for structural components. A schematic flowchart of the methodology proposed to address this task is given in Fig. 5.

Nonlinear dynamic analyses of three-dimensional finite element models set up in OpenSees [33] are used to determine the demand parameters for structural components. To account for the record-to-record variability, this study utilizes a suite of 400 synthetic ground motions provided through the stochastic ground motion predictive model by [63], calibrated using a subset of the NGA-West2 database. Furthermore, as shown in Fig. 6, the set of ground motions is accurately scaled to obtain a uniform distribution of the IM (peak ground acceleration) to adequately fit the fragility functions in high IM regions.

To properly account for uncertainties in materials, construction details, model, and seismic demand, 50 nominally identical but statistically different finite element models of bridges were considered. Details on the random parameters adopted for these uncertainties are given in Section 3. For each model, the suite of ground motions is applied within a nonlinear dynamic analysis, resulting in a sample size of 20 k demand parameters. The nonlinear behavior of structural components is taken into account for those considered as most vulnerable with respect to seismic and deterioration phenomena, i.e., COL, HTFB, HTEB, LTFB. Further details on the nonlinear behavior modeling and how corrosion effects are accounted for are given in Section 2.4. For each nonlinear dynamic analysis, structural component, and damage state, 50 capacity limit values are sampled aligning with the statistical thresholds defined in Table 2. These are subsequently compared with the resulting demand parameters, defining the SDSs exceeded by the component due to the seismic action, resulting in a total of 1M SDS labels for each structural component, achieved by the same number of IM. The obtained dataset is used to predict the probability of an SDS given an IM. In the studies of [3,67], the potential of nominal, ordinal, and hierarchical multinomial logistic regression and the softmax function to enhance fragility prediction by efficiently avoiding crossings of fragilities among damage states without including any parametric constraint has been highlighted. In this work, to allow for utmost flexibility of the learned fragility models, the nominal approach is adopted. Thereby, the fragility for a limit state SDS $= i$ is obtained through the sum of the softmax functions, at every timestep, related to the SDSs $\ge i$:

$$P(SDS \ge i \,|\, IM, CDS) = \frac{\sum_{j=i}^{J} e^{\beta_{0,j}+\beta_{1,j}\ln(IM)}}{\sum_{j=0}^{J} e^{\beta_{0,j}+\beta_{1,j}\ln(IM)}} \tag{17}$$

where J is the number of SDSs defined in Table 2, plus one, to consider the possibility of not activating any damage state.

The nominal state-dependent softmax-based fragility functions are derived for sixteen deterioration scenarios, obtained as a combination of the defined four CDSs (Table 2) with the number of deteriorating component typologies (i.e., COL and BEA). Results for the state-dependent fragility according to those scenarios for the four SDSs (Table 1) are given in Section 4.

2.4. Corrosion modeling of structural components

In bridge structural modeling, we assigned nonlinear behavior to the columns and bearings, due to their vulnerability to seismic events and sensitivity to corrosion phenomena. These components play a crucial role in ensuring structural safety, as failures within these elements can pose significant threats to the integrity of the entire structure.

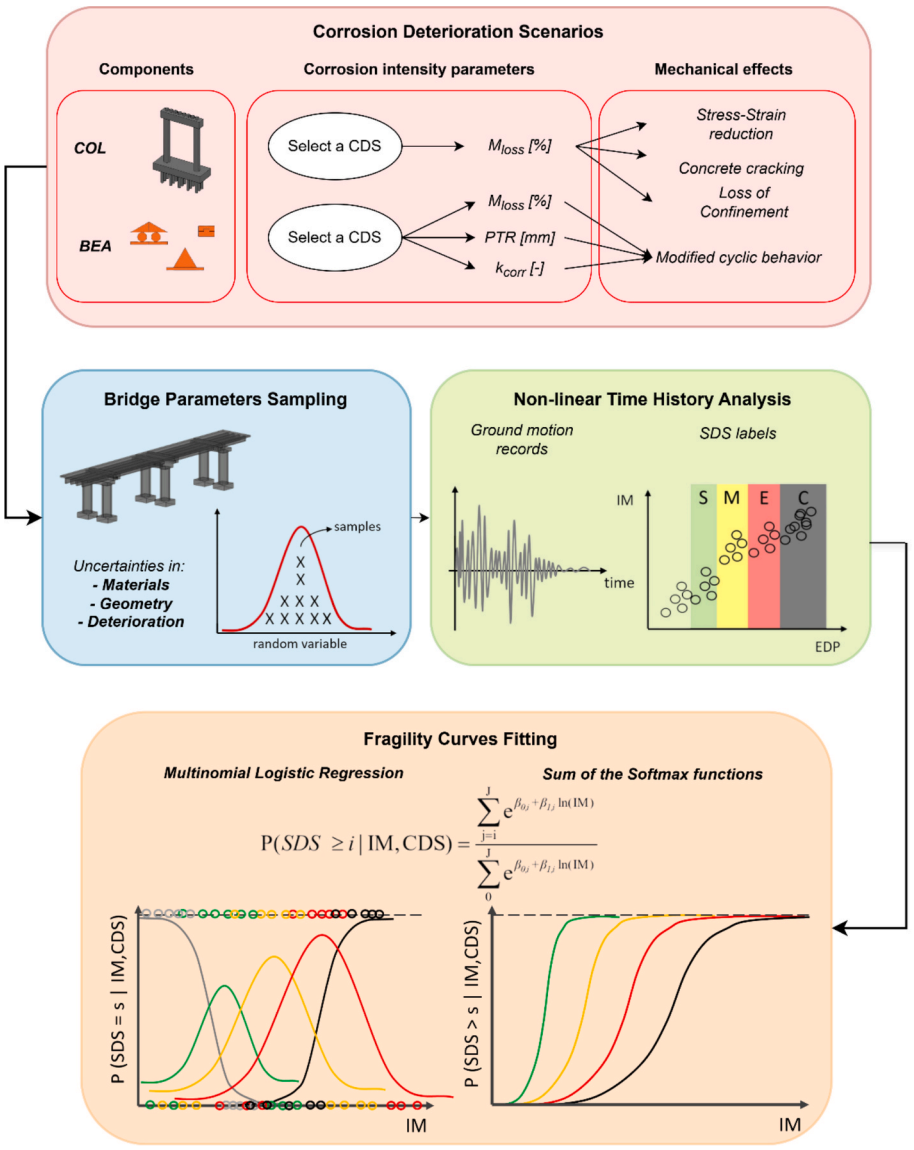

Fig. 5. Flowchart for the methodology to evaluate the state-dependent fragility curves.

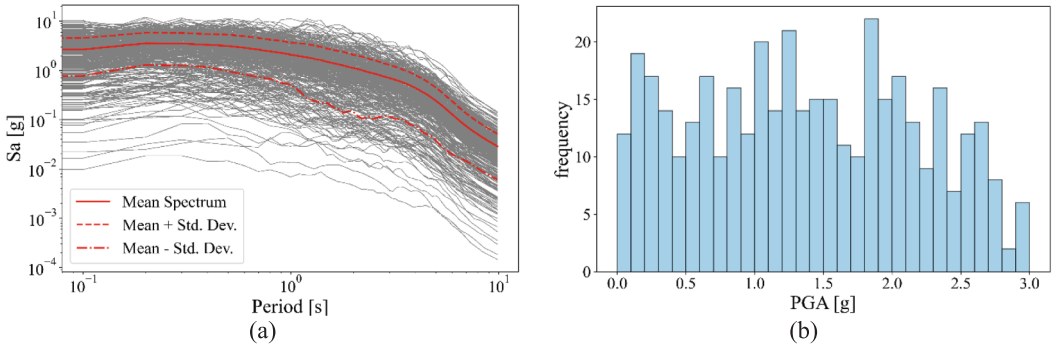

Fig. 6. Characteristics of the ground motion suite. a) Spectral acceleration vs. period; b) peak ground acceleration distribution.

Furthermore, in this study, three different steel bearings are considered, resulting in a total of 4 different components for which the nonlinear behavior is accurately modeled: COL, HTFB, HTEB, and LTFB.

Corrosion in columns not only reduces their lateral load-bearing capacity but can also lead to a decrease in stiffness or abrupt changes in inelastic behavior. Such alterations in behavior stem from a combination of factors which include (i) reductions of the steel rebar cross-sectional areas, which also involves modification of the steel strain–stress law due to micro-morphology aspects[26]; (ii) concrete cover cracking, spalling, and loss of steel–concrete bond due to corrosion oxide expansion; and (iii) loss of confinement action in the concrete cover due to stirrup corrosion. A comprehensive description of the

modeling assumptions made to account for these effects numerically in finite element analysis is presented along with a schematic overview in Fig. 7.

The nonlinear behavior of columns due to steel reinforcement corrosion has been considered in the numerical finite element model by reducing as a function of M_{loss} [%] the (i) reinforcement strength; (ii) concrete cover strength and stiffness; and (iii) concrete core confinement. Steel rebar and bolt yielding strengths have been reduced according to the degradation law for uniform and pitting corroded rebars proposed in [26], in which degradation relationship for the stress–strain law are derived from experimental data for both pitting and uniform corrosion of rebars. In this approach, the authors suggest using degradation relationships instead of the cross-sectional reduction to account for the morphological effects of the corrosion:

$$f_{y,corr,pit} = f_y(1 - 0.019961 * M_{loss}[\%]) \quad (18)$$

$$f_{y,corr,uniform} = f_y(1 - 0.0143453 * M_{loss}[\%]) \quad (19)$$

Note that the morphological nature of the corrosion is taken into account in this work by considering uniform corrosion law if pitting factor R is lower than 4, and pitting corrosion law if R is higher than 4, thus identifying the type of corrosion as suggested in [6]. Concrete cover cracking following the expansion of the oxides produced by the corrosion process is accounted as proposed in [16], by reducing the concrete cover compressive strength as:

$$f_c^* = \frac{f_c}{1 + K\varepsilon_1/\varepsilon_{c0}} \quad (20)$$

where K is a coefficient related to bar roughness and diameter, assumed equal to 0.1 for medium-diameter ribbed bars; ε_{co} is the strain at the peak compressive stress f_c; and ε_1 is the smeared tensile strain in the cracked concrete at right angles to the direction of the applied compression, evaluated as:

$$\varepsilon_1 = \frac{n^{\circ}_{bars} W}{D_c} \quad (21)$$

where D_c is the column diameter; and W is the average crack opening due to corrosion oxides expansion, estimated as proposed by [62]:

$$W = 0.0575 * \Delta A_{bars} \quad (22)$$

where ΔA_{bars} is the cross-sectional area reduction due to corrosion of the steel rebars. In [16], it is also suggested to consider the concrete cover stiffness reduction, which is accounted for in this work in a simplified but safety-aware way, by neglecting the presence of the concrete cover upon exceedance of an average crack width of 1 mm. The confinement of the concrete core compressive strength in columns is modeled through the Eq. (23), as proposed by [31]:

$$f_{cc} = f_c\left(-1.254 + 2.254\sqrt{1 + \frac{7.94k_e f_1}{f_c}} - 2k_e f_1 f_c\right) \quad (23)$$

This strength is expected to decrease since the corrosion of stirrups reduces the confinement action. This effect is accounted for by reducing the yielding strength of the stirrups.

The spatial distribution of degradation represents a crucial aspect in the structural modeling of a corroded RC structure. This concept emphasizes that corrosion does not occur uniformly across the entire structure or within an individual structural member. As noted by [68], the localization and the extent of degradation in a column can lead to unpredictable plasticity localization during seismic action (i.e., not just at the column base), consequently altering the column's failure mechanism. This aspect is considered in the modeling in a simplified manner: each column is discretized into 3 elements along its height. For each element, a corrosion intensity, in terms of the average rebars mass loss, M_{loss} [%], is randomly assigned accordingly to the range of the specific CDS class. This assumption allows variability of corrosion across the height in an approximate way, at the same time avoiding an excessively uneven distribution of corrosion within the same column.

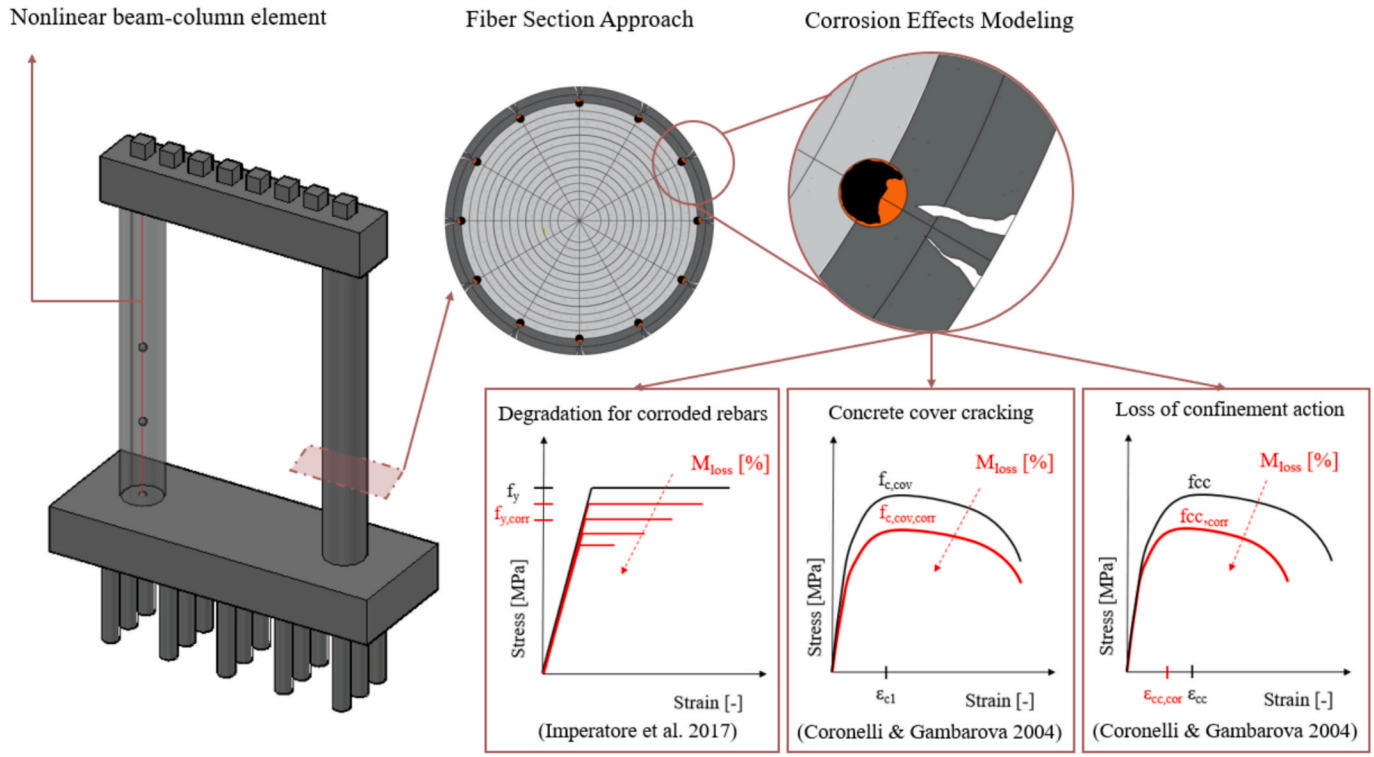

Fig. 7. Corrosion modeling assumptions in column components.

Fig. 8 shows the effects of corrosion on the cyclic behavior of circular RC columns. The cross-section of the column is the same as considered in the case study and further information about its features is given in Section 3. It is worth noting that the column's cyclic behavior is strongly modified by corrosion. Lateral bearing capacity is reduced with the increase of the corrosion effects, which are expressed in a synthetic way, through the average mass loss by the rebars M_{loss} [%]. Furthermore, the demand for the curvature ductility increases because of the stiffness and strength decay due to corrosion.

With regard to steel bearing components, various forms of degradation can occur. This study considers steel bearing components that could potentially suffer from (i) corrosion of anchor bolts in concrete/masonry pedestals; (ii) reduction in the thickness of steel plates; and (iii) accumulation of corrosion rust and debris on sliding surfaces, all of which can adversely impact their nonlinear behavior. Three types of steel bearings are considered in this study: HTFB, HTEB, and LTFB. The numerical modeling approach for these is largely based on the extensive study by [30], in which the experimental behavior of several types of steel bearings is compared with analytical methods and valuable suggestions for finite element modeling are reported. That study is also referenced in [23,53], where the corrosion effects on these components are introduced in time-dependent fragility analysis for aging bridges. Following these approaches, the mechanical behavior of these components is studied and modeled separately with regard to the longitudinal and transverse direction of the bridge. The failure mechanisms that characterize these critical components, along with the description of their corrosion effects and the modeling assumptions to capture their cyclic behavior, are summarized in Fig. 9 and described in the following.

Failure of the HTFBs in the longitudinal direction is governed by the bolt prying mechanism in the masonry/concrete plate (Fig. 9.a). The ultimate force is:

$$F_{l,ult} = \frac{0.5 b_l N}{h}\left[\left(1+\frac{nT}{N}\right) - \frac{N}{0.85 f_c b_l b_t}\left(1+\frac{nT}{N}\right)^2\right] \quad (24)$$

where N is the normal load to the bearing; b_l is the width of masonry plate and bedding material; h is the height of the bearing from the concrete pedestal to the sole plate-rocker interface; n refers to the number of anchor bolts; and b_t is the width of masonry plate in the transverse direction. In Eq. (24) the considered pulling action T is the minimum between the failure due to the yield strength of the bolts, Eq. (25), and bond failure in bolts, Eq. (26):

$$Y = A_{b,pit} f_{yb} \quad (25)$$

$$B = b_u \pi d_{b,uni} l_d \quad (26)$$

where $A_{b,pit}$ is the cross-sectional area of the bolt considering pitting corrosion; f_{yb} is the yielding strength of the bolts; $d_{b,uni}$ is the bolt diameter considering uniform corrosion; l_d is the bolt's embedment length; and b_u is the bond stress between the bolt and the concrete, assumed constant for the sake of simplicity. The HTFB cyclic behavior is modeled in OpenSees through friction (i.e., "Steel01 material") and hysteretic (i.e., "Hysteretic material") links (Fig. 9.b), as suggested in [30]. Corrosion effects are considered in evaluating the yield strength, Eq. (25), and the bond strength of the bolts, Eq. (26). Regarding the yielding strength, in [53], the "necking" effect at the concrete interface is pointed out as a serious threat for the bearings. This corresponds to a localization of section reduction due to dissimilar environments because of concentration cell corrosion. However, in [53], experimental on-field data were used to consider this effect while calculating the ultimate strength of fixed bearings in the longitudinal direction. In the absence of precise data, this study suggests adopting a pitting factor to account for this localized section reduction.

The steel HTEB are devices that, in the longitudinal direction, accommodate the displacements imposed by the mechanical or thermal deformations affecting the bridge deck (Fig. 9.c). The mechanical behavior is thus modeled in OpenSees through "Steel01" material link characterized by a friction coefficient evaluated as:

$$\mu_l = 0.04 + 0.08 k_{corr} \quad (27)$$

in which the effect of interlocking between contact surfaces due to bearing corrosion is accounted for through the k_{corr} parameter, defined in Table 2 as a function of CDSs. In the transversal direction, both the HTFBs and the HTEBs have the functional purpose of constraining the transverse displacements (Fig. 9.e). This behavior is modeled in OpenSees through friction (i.e., "Steel01 material") and hysteretic (i.e., "Hysteretic material") links (Fig. 9.f), as suggested in [30]. The failure modes for these components in the transverse direction are defined by the failure of the steel plate, Eq. (28), and the shear failure in anchor bolts, Eq. (29):

$$P = 2\left(\frac{t_{p,corr}^2}{4} f_{su} + \frac{(0.707 t_{w,corr})^2}{4} f_{su}\right)\left(\frac{L_x}{L_y} + \frac{2L_y}{L_x}\right) \quad (28)$$

$$SF = n_b A_{b,pit} f_{shb} \quad (29)$$

where $t_{p,corr}$ and $t_{w,corr}$ are the time-dependent thickness of the keeper plate and fille weld; f_{su} is the ultimate strength of the keeper plate; L_x and L_y the length and breadth of the keeper plate; and f_{shb} the shear strength of the bolts. Over time, the steel plate is subjected to thickness reduction at its exposed boundary during the lifetime of the structure. To account for this, given a CDS, the plate thickness reduction (PTR [mm]) value is sampled considering a uniform distribution where the lower and upper bound are as defined in Table 2. The shear failure of bolts is exacerbated by the "necking" effect at the bolt-concrete pedestal interface. To account for this effect, the cross-sectional area considered in the calculation accounts for a pitting reduction, as previously explained for the yielding failure ($A_{b,pit}$).

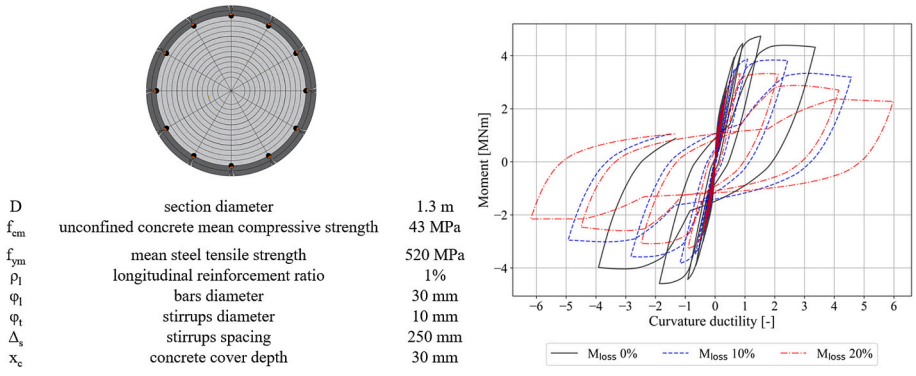

D	section diameter	1.3 m
f_{cm}	unconfined concrete mean compressive strength	43 MPa
f_{ym}	mean steel tensile strength	520 MPa
ρ_l	longitudinal reinforcement ratio	1%
φ_l	bars diameter	30 mm
φ_t	stirrups diameter	10 mm
Δ_s	stirrups spacing	250 mm
x_c	concrete cover depth	30 mm

Fig. 8. Cyclic behavior of column components under uncorroded and corroded cases.

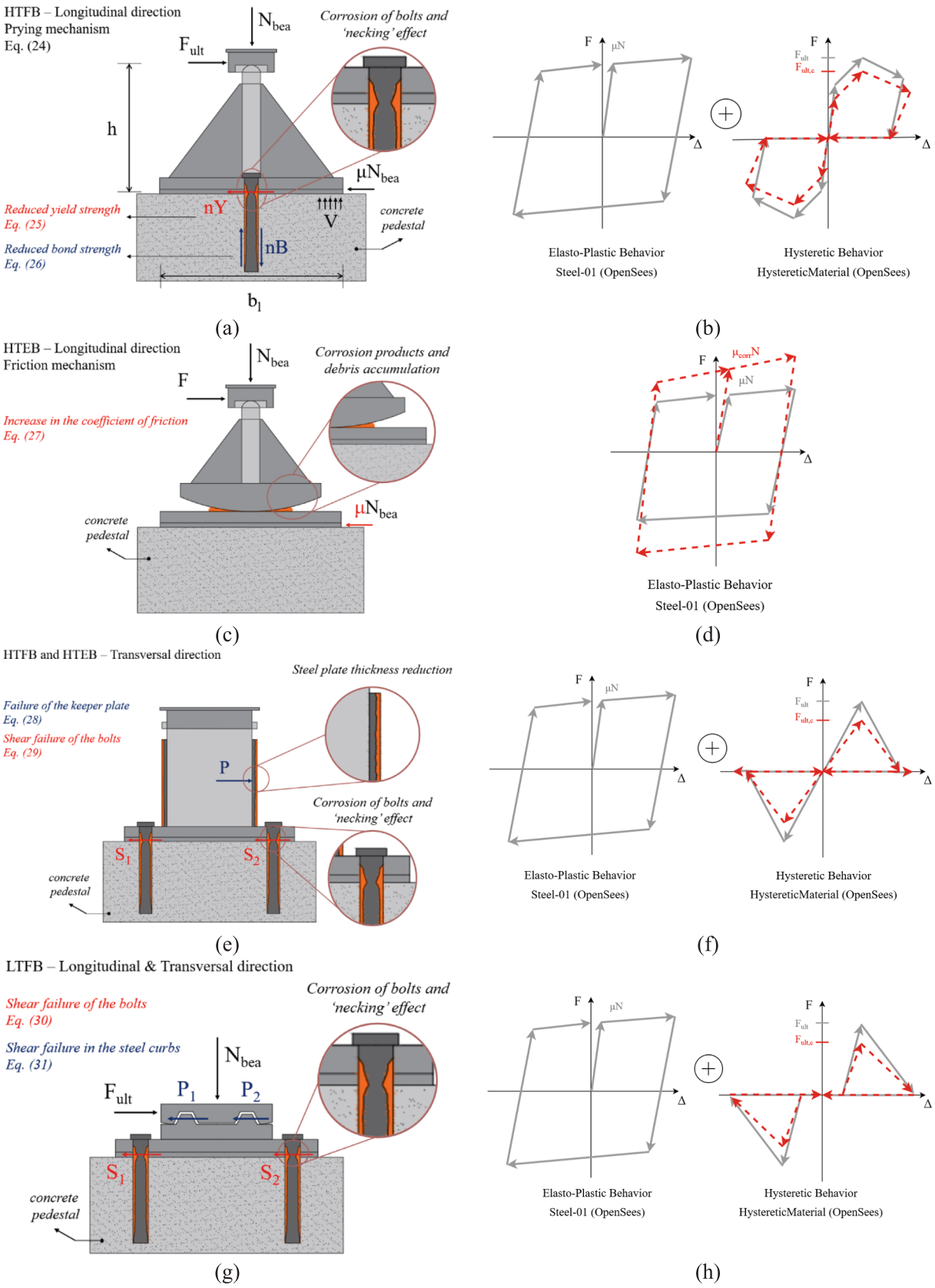

Fig. 9. Corrosion modeling assumptions in bearing components, modified according to [53].

The LTFB behavior is the same for the longitudinal and transversal directions (Fig. 9.g). The behavior is modeled in both cases through "Steel01" and "Hysteretic" links in OpenSees (Fig. 9.h). These are characterized by two following failure modes, namely, shear failure in the bolts, Eq. (30), or failure of the steel curbs, Eq. (31):

$$B_{LTFB} = n_b A_{b,pit} * 0.6\, f_{yb} \tag{30}$$

$$C_{LTFB} = n_c A_c f_{su} \tag{31}$$

where n_c represents the number of steel curbs; A_c cross-section area of a curb; and f_{shu} is the ultimate strength of the steel curbs. Corrosion effects are supposed to reduce the shear strength of the bolts due to the "necking" effects at the concrete interface, again considered through the pitting factor $A_{b,pit}$.

Fig. 10 shows an example of the effects of corrosion on the cyclic behavior of the considered bearing typologies under a constant axial load of 356 kN. Corrosion results in reductions in the lateral capacity of bearing components for all the mechanisms, except for the HTEB longitudinal behavior, where corrosion debris increases the coefficient of friction. It can be noted that the intensity of the reduction in the bearing capacity is different among components, since different corrosion effects and failure mechanisms are considered.

The described modeling approach is thus used in finite element analysis to evaluate state-dependent fragilities. In summary, according to a corrosion scenario, which is a combination of CDSs characterizing the two component typologies (i.e., COL and BEA), the corrosion intensity parameters are sampled concerning the CDS of the component typology according to the ranges defined in Table 2 and following a uniform distribution. For column elements, the M_{loss} parameter and the pitting factor R are assigned, and then, the fiber mechanical properties of "Nonlinear Beam Column Element" (OpenSees) are reduced. For the bearing components, the M_{loss} [%], PTR [mm], and the k_{corr} [-] are sampled accordingly. From M_{loss} [%], the average cross-sectional area ($A_{b,uni}$) and diameter ($d_{b,uni}$) of the bolt are obtained considering a uniform reduction. Then, considering a pitting factor R, sampled again using Gumbel distribution [58]), the bolt minimum diameter ($d_{b,pit}$) at the necking interface is determined. On the other hand, for the bond strength, uniform average reductions in the diameter ($d_{b,uni}$) are considered to account for the degradation of the bond strength, since this depends on the whole contact surface between steel and concrete. PTR [mm] reflects the geometrical reduction of the thicknesses for the steel plates (t_p and t_w), and the k_{corr} [-] parameter directly affects the coefficient of friction of expansion bearing as in Eq. (27).

3. Case study bridge

The methodology described in the previous section is applied to a pre-70 s archetype 4-span bridge, representing a wide range of seismic-vulnerable and deterioration-sensitive existing reinforced concrete bridges in infrastructure networks. The main geometrical features and finite element modeling choices are summarized in Fig. 11. The deck has eight prestressed I-beams, 1.5 m high, and forms two Gerber spans

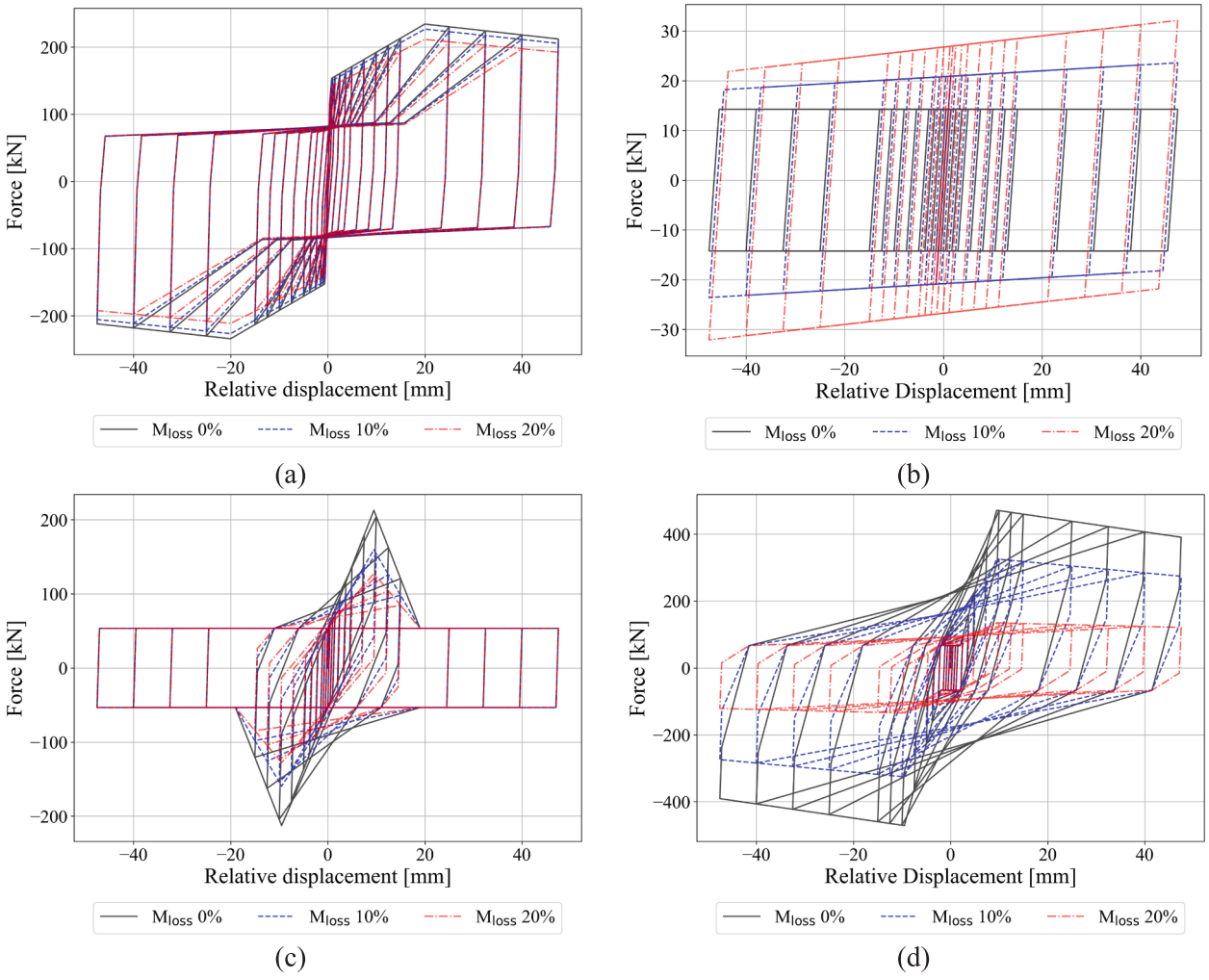

Fig. 10. Cyclic behavior of bearing components under uncorroded and corroded cases.

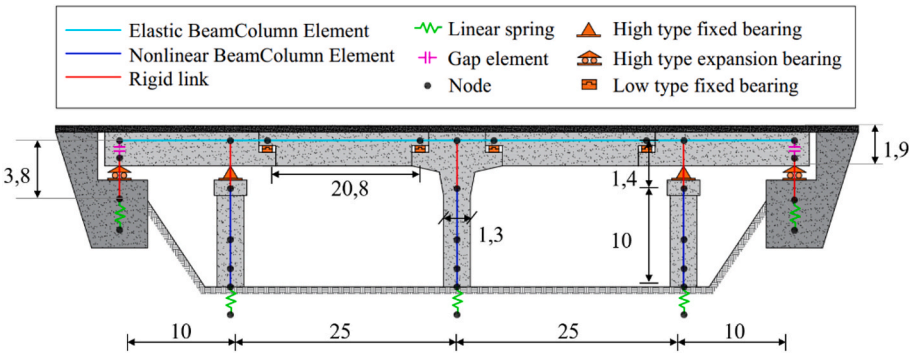

Fig. 11. The 4-span bridge case study with respective geometrical and finite element modeling features. Modified after [36].

between half-joints. The deck is supported by three double-pier bents, 10 m high with circular cross-section of 1.3 m diameter. Seismically vulnerable features of the bridge include the poor detailing of the columns, with a longitudinal reinforcement ratio of 1 % and a circular stirrup spacing of 250 mm, without any additional confinement in the dissipative zone. Furthermore, the presence of steel bearings represents a structural weakness against seismic actions: HTFBs are placed at the column-deck connection, HTEBs are placed at the deck-abutment connection, and LTFBs are used for the cantilever and half joints. Moreover, the supported beam scheme itself has been shown to be particularly vulnerable in real earthquakes as it allows for possible unseating of the span.

In fragility analyses of bridges, superstructures are usually expected to remain elastic during the earthquake and, therefore, model nonlinearities are considered only for the most vulnerable components of the structure [41]. For this reason, the deck is modeled with linear elastic beam column elements in OpenSees. For columns, nonlinear beam-column elements are used with appropriate (un)confined concrete and steel properties in OpenSees. The structural component is discretized along the height into three distinct elements. This way, since wide value ranges for CDSs are considered (Table 2), the chance to have different corrosion intensity (M_{loss}) within the same CDS along the height of the column is captured, thus the possibility of plastic hinges in zones away from the column base due to corrosion is reproduced [68]. According to [30] and [53], the behavior of the bearings is modeled through a combination of friction and hysteretic links in the direction where displacements are constrained, and friction links only in the longitudinal direction for HTEB, as explained in the previous section. Pile foundations are modeled using soil-foundation springs with linear behavior, and abutments are modeled with linear translational springs, considering both passive and active stiffnesses. Abutment-deck gaps are modeled trough gap elements. Regarding the bridge sampling, the random variables considered to propagate the uncertainties in the materials and the finite element modeling are summarized in Table 3.

Following the definitions of [20], the environmental effects of both "splash" zone, which can be representative also approximately of regions affected by the use of de-icing salts, and "atmospheric" zone are considered in the analysis to show the longitudinal life-cycle effects on seismic fragility of two different environments. Moreover, "humid" exposure is considered. Accordingly, the random parameters for the propagation of uncertainties in the assessment of non-stationary transitions among CDSs for the case study bridge components are summarized in Table 4.

4. Results

This section presents the results derived from applying the methodology delineated in Section 2 to the case study detailed in Section 3. We focus on three primary outcomes: (i) the non-stationary transitions of the CDSs for the bridge components according to "splash" and "atmospheric" conditions; (ii) the time-invariant and state-dependent fragilities for structural components according to sixteen unique deterioration scenarios (combinations of the 4 distinct CDS with 2 different component typologies, COL and BEA); and (iii) the system and component life-cycle fragility evolution, as obtained by integrating the transitions through the proposed dynamic Bayesian network of Section 2.1.

4.1. Components CDSs transition matrices

Figs. 12 and 13 visually represent the non-stationary transition matrices, illustrating the impact of chloride corrosion under "splash" and "atmospheric" environmental conditions, respectively. Each matrix encapsulates the Markovian transition probability from state i to state j over the time interval t to $t+1$. Considering that damage is irreversible, therefore components cannot transition from more severe to milder corrosion states, these matrices are upper-triangular under the

Table 3
Random variables for bridge modeling.

Parameter	Units	Distribution	Mean	St. dev.	CoV	l.b.	u.b.	Ref.
f_c Conc. compressive strength	[MPa]	Nor.	43	8.6	20 %			–
ε_{cu} Conc. ultimate compressive strain	[-]	Log.	0.008	0.0008	10 %			[17]
ε_{ccu} Conf. Conc. ultimate compr strain	[-]	Log.	0.03	0.003	10 %			[17]
E_c Contrete elastic modulus	[MPa]	Nor.	34,962	6992	20 %			[17]
f_y Yield strength of steel	[MPa]	Log.	520	52	10 %			–
E_s Steel elastic modulus	[MPa]	Nor.	$2*10^5$	4000	2 %			–
x_c Concrete cover depth	[mm]	Log.	30	6	20 %			[52]
Bearing coefficient of friction factor	[-]	Nor.	1	0.1	10 %			–
Stiffness of soil-foundation springs	[kN/mm]	Uni.			–	28	84	[41]
Abutments passive stiffness	[kN/mm/m]	Uni.			–	11.5	28.8	[41]
Abutments active stiffness	[kN/mm/m]	Uni.			–	3.5	10.5	[41]
Abutment-deck gaps	[mm]	Nor.	38.1	1.1	3 %			[41]
Damping ratio	[-]	Nor.	0.045	0.013	29 %			[41]
Mass multiplicative factor	[-]	Uni.			–	0.9	1.1	[41]

Table 4
Random variables for corrosion initiation and propagation.

Parameter	Units	Distribution	Condition	Values	Mean	St. Dev.	a	b	Ref.
Zone	[-]	Det.	Bearings	Splash					–
			Columns	Atmospheric					–
Exposure	[-]	Det.	–	humid					–
Bar diameter	[mm]	Det.	Bearings	25					–
			Columns	30					–
χ	[-]	Log.	–	–	1.00	0.05			[12]
C_s	[% binder]	–	$Cs = Acs + \varepsilon cs$	–					[12]
A_{cs}	[-]	Nor.	splash zone	–	7.758	1.36			[12]
			atmospheric zone	–	2.565	0.356			[12]
ε_{cs}	[-]	Nor.	splash zone	–	0.00	1.105			[12]
			atmospheric zone	–	0.00	0.405			[12]
x_c	[mm]	Log.	–	–	30	6			[52]
w/c	[-]	Uni.	–	[0.40; 0.45; 0.50]	–	–			–
C_{cr}	[% binder]	Nor.	wc = 0.40; humid	–	0.80	0.10			[12]
			wc = 0.45; humid	–	0.85	0.125			[12]
			wc = 0.50; humid	–	0.90	0.15			[12]
D_0	[mm^2/year]	Nor.	w/c = 0.40	–	220.90	25.40			[12]
			w/c = 0.45	–	315.60	32.50			[12]
			w/c = 0.50	–	473	43.20			[12]
a	[-]	Beta	atmospheric zone	–	0.65	0.07	0	1	[20]
			splash zone	–	0.37	0.07	0	1	[20]
b_e	[-]	Nor.	–	–	4800	700			[52]
T_{real}	[°K]	Nor.	–	–	293	5			–
R	[-]	Gum.	phi<=20	–	6.20	1.12			[58]
			phi > 20	–	7.10	1.21			

assumption that no structural interventions are provided.

The orange curves of Fig. 12 and the blue curves of Fig. 13 represent the time-dependent probability of transitioning from a CDS = *i* at time t to a CDS = *j* at time $t + 1$. It must be emphasized that, when considering a 100-year structural lifespan, corrosion initiation was observed in 97.1 % of the samples exposed to "splash" conditions, while only in 2.7 % of the samples under "atmospheric" conditions, which underscores the significance of correct exposure identification with respect to these two environmental conditions. The derived statistical results from the corrosion initiation model are assumed to display characteristic lognormal distributions for the corrosion-activated cases. Specifically, the time to corrosion initiation (T_{corr}), corresponding to a mean concrete cover depth of 30 mm, under "splash" conditions has a mean value of 13.7 years with a standard deviation of 20.7 years. In contrast, under "atmospheric" conditions, the mean T_{corr} extends to 98.6 years, with a standard deviation of 9.6 years. These observations substantially influence the transition probabilities associated with both the initiation phase of the phenomenon (i.e., from CDS = 0 to others) and the propagation phase transition probabilities (i.e., other transitions). In the case of "splash" zone, sharp inflection points are observed for the transitions to $CDS_{t+1} = 0$ from $CDS_t = 0$ and to $CDS_{t+1} = 1$ from $CDS_t = 0$. Indeed, the statistics of T_{corr} under these conditions indicate that the onset of corrosion is more likely in the early years of the life cycle. Similarly, an inflection is observed for the same transitions related to the "atmospheric" zone, shown in Fig. 13 (blue curves), yet the effect is mitigated due to the characteristics of the T_{corr} variable assumed for these conditions. Additionally, in both Figs. 12 and 13, another trend is noticeable for the transitions from $CDS_{t+1} = 1$ to $CDS_t = 1$ and $CDS_{t+1} = 2$ to $CDS_t = 2$. For these, the probability of remaining in the same corrosion state increases over time. This trend is attributed to two factors. First, the corrosion propagation law, Eq. (10), features a decreasing trend with respect to the difference (t-T_{corr}). As a result, the farther from the onset of corrosion, the slower the corrosion rate and its variability according to the assumptions adopted in the Gamma process. Secondly, the assumed ranges of CDSs in terms of corrosion intensity affect the probability of annual transitions from a CDS to the next. It is thus highlighted that with different assumptions regarding the range definitions for CDS or different corrosion propagation laws, the shapes of these time-dependent transition curves might vary.

Finally, a further trend can be observed in the transition probabilities of Figs. 12 and 13. When corrosion is already active ($CDS_t \geq 1$), the conditional probabilities of progressing to higher CDSs are greater under atmospheric exposure than under splash exposure. This effect follows directly from the corrosion propagation law of Eq. (10), which decreases with the elapsed time ($t - T_{corr}$) and is identical to both environments. Since the mean T_{corr} is much lower under splash conditions compared to the atmospheric one, the elapsed time at any time point is higher, therefore the propagation *rate*, thus the transition probability, is lower. The higher transition probability related to the atmospheric condition should not be misinterepreted as the probability of attaining advanced corrosion states when integrating over the structure's lifetime. Indeed, at first glance, non-stationary transitions might not illustrate the evolution of environment deterioration. In Fig. 14, we present the probabilities of components belonging to a certain state for both environmental conditions, as computed by a forward evaluation of the Markovian transitions, employing Eq. (4). The comparison is quite intuitive, revealing that the probability of encountering higher deterioration conditions is predominantly associated with "splash" conditions.

4.2. Components state-dependent fragility curves

Figs. 15–18 display the case study bridge's time-invariant and state-dependent fragility curves. These functions delineate the probability of exceeding the defined (Table 1) seismic limit states (i.e., Slight, Moderate, Extensive and Complete) in relation to the intensity measure and several deterioration scenarios, which are defined as combinations of the CDSs for structural components, and denoted by a two-digit code, where the first digit refers to the CDS of the COL and the second one to the CDS of BEA components. The graphical representation offers an exhaustive overview of the seismic safety concerning the structural components and the system. Indeed, utilizing a multi-component approach allows us to distill the fragility characteristics across varying limit states of different components, which is integral for identifying the most seismically sensitive components within the bridge system.

Results are obtained by applying the proposed methodology (Section 2) to the case study (Section 3). It can be noted that the HTEB components exhibit the most pronounced fragility across the SDSs, with column components ranking next. In lower intensity measure values of less than 0.5g, it is observed that LTFB components can be dominant for the system fragility, especially in Slight and Moderate states. Comparing

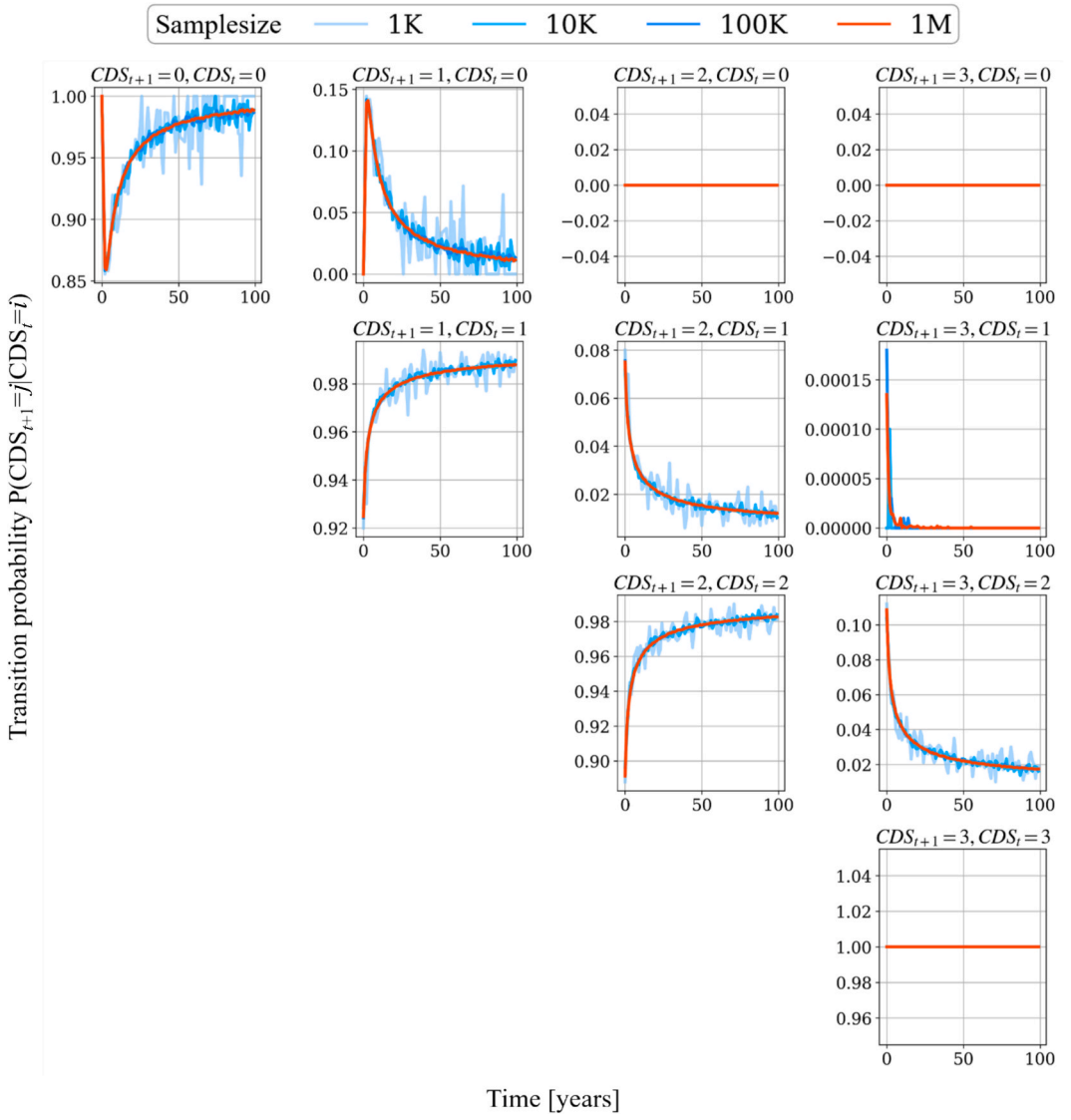

Fig. 12. Non-stationary transition matrix for CDS of components under "splash" conditions.

fragility functions across states for each component, we observe column components to be particularly sensitive to deterioration. Moreover, in deterioration scenarios where the degradation predominantly afflicts column components over support components, there is a considerable increase in the fragility of the columns, in some cases (e.g., scenario 30, Complete limit state), where COL fragility even surpasses HTEB fragility.

This increase is due to the influence of non-uniform distribution of deterioration over the structural components, which can engender significant alterations in the hierarchy of component strengths (or resistances) as demonstrated in prior studies [35]. This peculiar phenomenon in aging multi-component bridge structures is subject to further scrutiny in Appendix B where the structural mechanisms involved and the emphasis on alterations in the component hierarchy resulting from corrosion scenarios are elucidated.

Conversely, in deterioration scenarios where corrosion affects mainly the bearings rather than the columns (e.g., Scenario 03), a slight reduction in column fragility is observed, particularly for higher IMs. This behavior stems again from the altered hierarchy of component: the corrosion-induced mass loss in the bearings leads to yielding at lower stress and a partial decoupling of the superstructure mass from the columns. As a consequence, the seismic demand in the columns is reduced, resulting in lower deformations and, therefore, lower fragility. This important inter-component effect under uneven corrosion patterns is not possible to capture without a multi-component modeling approach. Further consideration on the non-linear interplay between components is given in Appendix B.

In Fig. 19, the varied fragility curves of SYS are depicted, corresponding to the sixteen corrosion scenarios under consideration. As delineated in Section 2, these curves are derived from a series system assumption. Specifically, for each set of individual non linear time history results, the SDS of the entire bridge system is inferred as being equivalent to the most severe of its components. Consequently, the fragility curves for both individual components and the overall system are generated using multinomial logistic regression, formulated as the sum of softmax functions as per Eq. (17). This analysis is conducted independently for each component and the system, leading to fragility curves with distinct dispersion. Under certain circumstances, the fragility curves of the system may slightly intersect with those of its individual components. This is a numerical artifact of the fact that system and component curves are fitted independently. For readers interested in exploring different methodologies for determining system fragilities, for example, with the matrix-based system reliability (MSR) method [57], Appendix A provides the regression coefficients for all components and the system pertaining to the four SDSs and the sixteen corrosion scenarios examined.

Finally, it is worth highlighting that the functions presented in

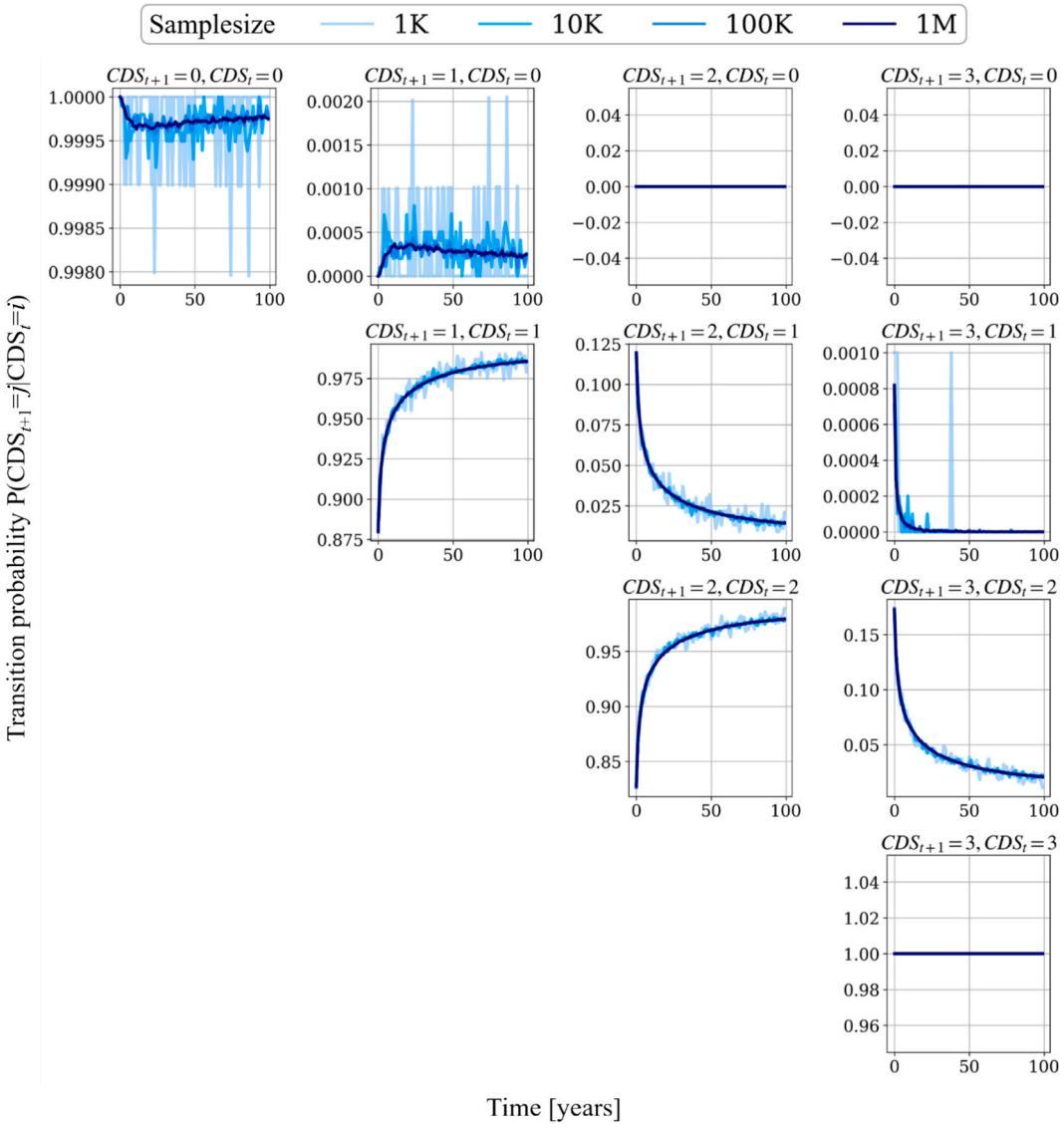

Fig. 13. Non-stationary transition matrix for CDS of components under "atmospheric" conditions.

Figs. 15-19 are independent of the temporal assessment of the corrosion state, and this aspect is believed to be of paramount importance in the context of life-cycle seismic safety evaluation and management. That is, these fragility functions are valid even when observation from on-site inspections and monitoring presents a corrosion scenario deviating from that predicted by the degradation models. This characteristic underscores the critical role of updatability in this approach.

4.3. System fragility curves

The longitudinal fragility of the bridge system is determined by combining the state-dependent system fragility of Fig. 20 with the probabilities of structural components existing in a particular state of deterioration (as shown in Fig. 14 through the proposed DBN. The network is implemented in a Python environment without the use of any existing toolbox. By adopting Eq. (32), in which, according to Eq. (4), the probability of having a given corrosion scenario (combination of CDS for COL and BEA component types) is expressed as eq. (33).

$$\mathrm{P}_t(\mathrm{SDS} \geq s\,|\mathrm{IM}) = \sum_{\mathrm{CDS_{COL}}} \sum_{\mathrm{CDS_{BEA}}} \mathrm{P}(\mathrm{SDS} \geq s|\mathrm{IM},\ \mathrm{CDS_{COL}},\ \mathrm{CDS_{BEA}})\mathrm{P}_t(\mathrm{CDS_{COL}}, \mathrm{CDS_{BEA}}) \tag{32}$$

$$\mathrm{P}_t(\mathrm{CDS_{COL}}, \mathrm{CDS_{BEA}}) = [\mathrm{P}_0(\mathrm{CDS_{COL}}) \prod_{\tau=0}^{t-1} \mathrm{P}(\mathrm{CDS_{COL},\tau+1}|\mathrm{CDS_{COL},\tau})][\mathrm{P}_0(\mathrm{CDS_{BEA}}) \prod_{\tau=0}^{t-1} \mathrm{P}(\mathrm{CDS_{BEA},\tau+1}|\mathrm{CDS_{BEA},\tau})] \tag{33}$$

To map the evolution of longitudinal fragilities, computations are performed at four time-points throughout the structural lifespan: at the as-built condition (0 years), and subsequently at 25, 50, and 100-year time-

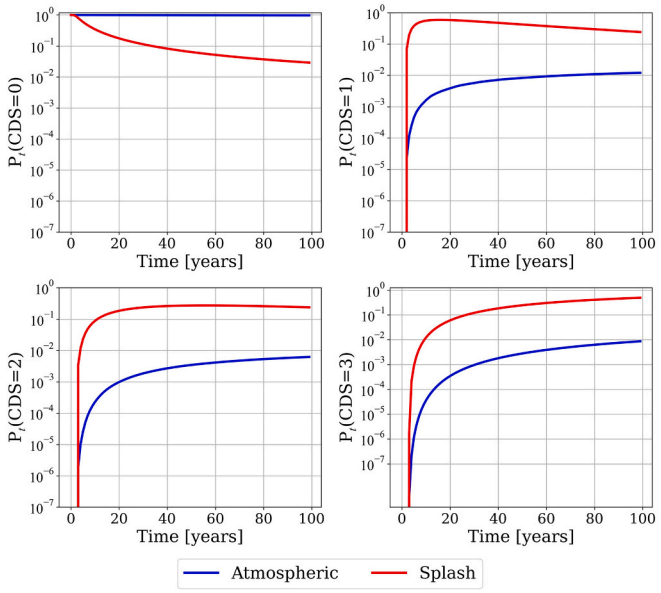

Fig. 14. Probabilities of corrosion deterioration states (P_{CDS}) of structural components over their lifetime.

points.

Fig. 20 presents these results, corresponding respectively to the Splash (Fig. 20.a, 20.b, 20.c) and Atmospheric conditions (Fig. 20.d). The comparison of these figures underscores again the pronounced influence of environmental conditions on the life-cycle fragility of the structure. Particularly noteworthy is the observation that Splash conditions trigger substantial modifications in fragility curves from 25 years of structural lifespan. In contrast, even after 100 years, the fragility increments under Atmospheric conditions appear negligible.

As corrosion progresses, component capacity decreases, and the following inequality is expected to hold for every IM: *P*(DS exceedamce | higher corrosion) $\geq$ *P*(DS exceedance | lower corrosion). Therefore, a leftward shift is observed for the curves (yielding a steeper profile esepcially in the low-to-moderate IM range, for lower damage states). Under severe corrosion scenarios, the probability of exceeding slight damage rises sharply at small IM values, concentrating the response within a narrower IM interval and steepening the corresponding fragility branch.

Another noticeable aspect is the differential impact of corrosion on the four damage thresholds. Specifically, for the Slight SDS, there are only minor increases in fragility over time. This is since, for the case study bridge, the as-built condition, already exhibits several seismic-prone features. Therefore, the exacerbating effects of corrosion on the nonlinear behavior of the structure lead to increased probabilities of

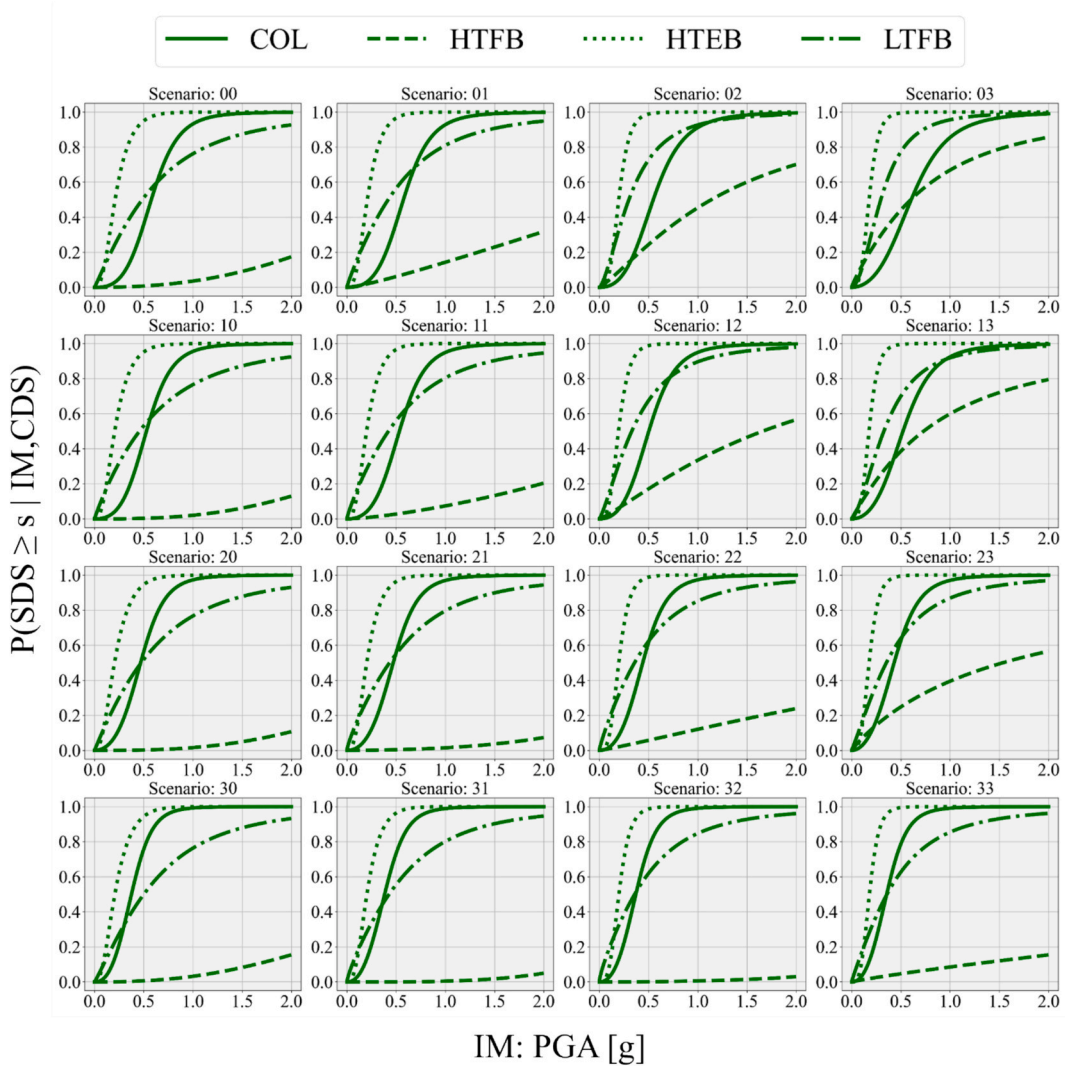

Fig. 15. State-dependent fragilities for the Slight SDS of the case study bridge components according to 16 scenarios. Scenario ij: i = CDS_{COL}, j = CDS_{BEA}.

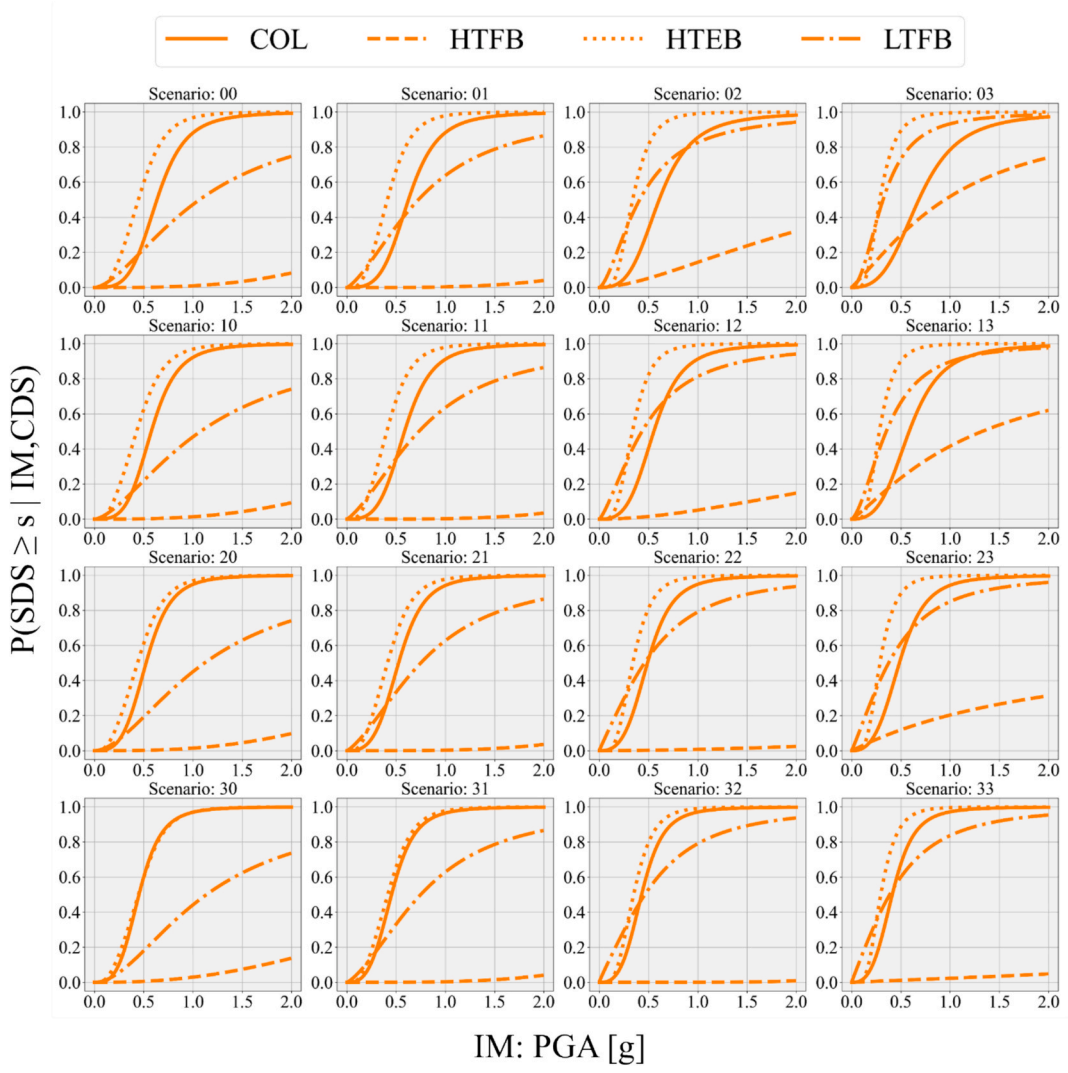

Fig. 16. State-dependent fragilities for the Moderate SDS of the case study bridge components according to 16 scenarios. Scenario ij: i = CDS_{COL}, j = CDS_{BEA}.

exceedance for certain states, particularly the Moderate and Extensive ones. Moreover, the bridge's fragility demonstrates an increasing trend over time, due to the increasing probability of experiencing higher deterioration states over time, as previously illustrated in Fig. 14. These findings demonstrate the capacity of the proposed methodology to account for the complex interplay between corrosion deterioration states and various structural components' damage in defining the system risk.

5. Discussion

In this section, we highlight and summarize several key insights in using the proposed DBN approach, which encapsulates the deterioration in discrete CDSs, couples Markovian non-stationary transitions and state-dependent fragility functions to provide comprehensive assessment of seismic safety, especially from the perspective of managing aging bridges.

First, applying the methodology allows us to evaluate individual bridge components' fragility, which is necessary for identifying the most vulnerable components across deterioration scenarios (for our case study these are the HTEB and COL components). Understanding the contribution of each component to the overall seismic fragility is a crucial piece of information for devising seismic retrofit intervention plans. It underscores the significance of the multi-component approach to the possibility of enhancing seismic safety, offering a nuanced and targeted analysis compared to single-component/full-system methodologies. Moreover, examining the sensitivities of individual components to degradation phenomena and their manifestation in seismic responses, enables a profound understanding of the sensitivity of the overall system fragility against possible deterioration combinations. Our approach is capable of unravelling the interplay of degradation mechanisms and strength hierarchies within the system, facilitating, for instance, the evaluation of how corrosion differentially impacts COL and HTEB components, and which one triggers predominant failure mechanisms for different IMs, and what is the overall outlook at the macro-level of system fragility over the structural life-cycle. Disentangling complex effects related to the interplay of the most vulnerable components depending on different exposure conditions and deterioration scenarios with a full spectrum of risk information is of paramount importance for the capability to steer structural intervention decisions.

To illustrate this point further, an additional evaluation of the deterioration effects on the seismic safety is presented in Fig. 21, where the fragility of the components COL, HTEB, and the SYS are plotted according to scenarios 00 (As-built), 03 (maximum corrosion in bearings, none in columns), 30 (no corrosion in bearings, maximum in columns), 33 (maximum corrosion in both bearings and columns). Naturally, results reveal that maximum fragility is consistently observed when corrosion is widespread across the structure for both these components and the system (e.g., red curves in Fig. 21a-c). However, it is

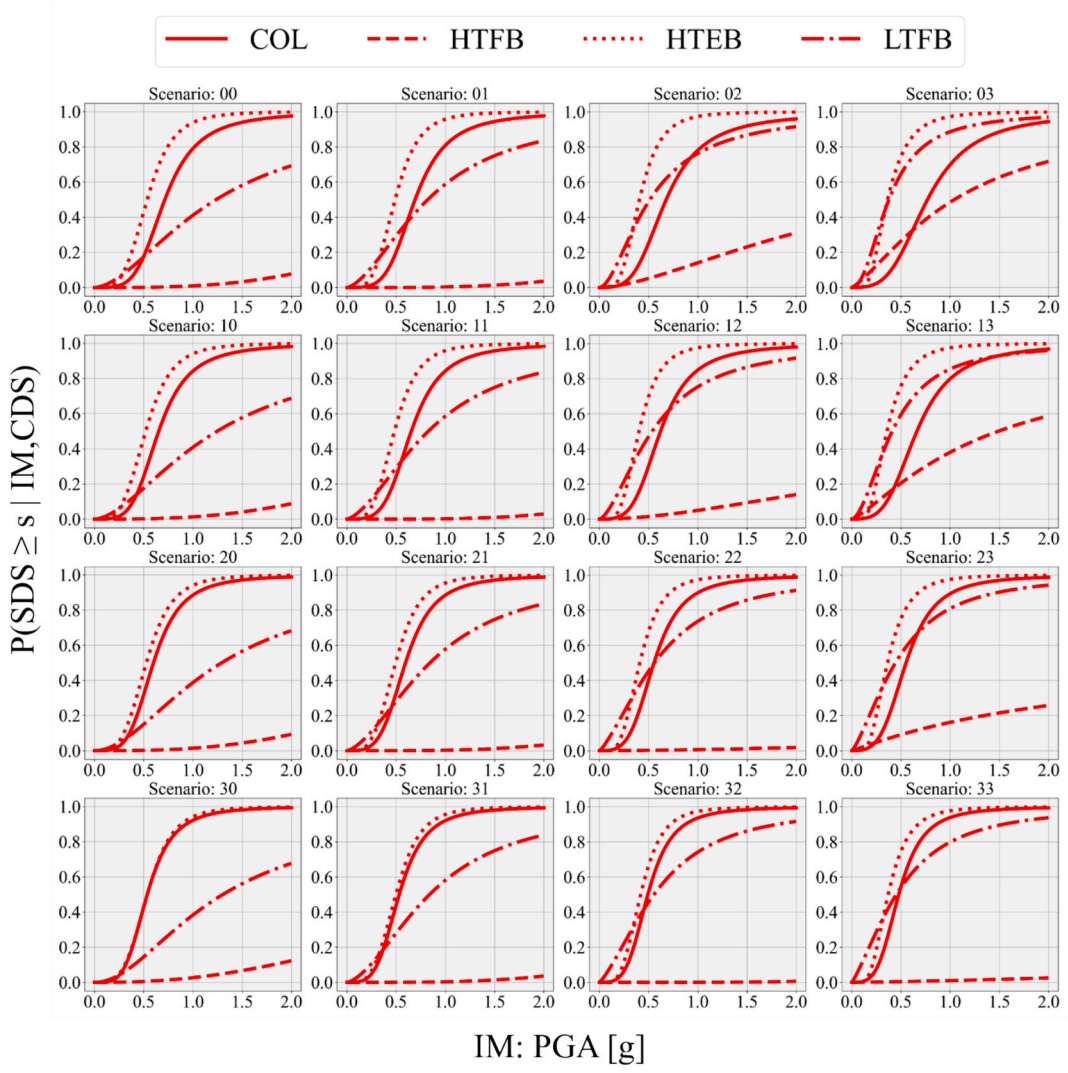

Fig. 17. State-dependent fragilities for the Extensive SDS of the case study bridge components according to 16 scenarios. Scenario ij: i = CDS_{COL}, j = CDS_{BEA}.

noted that columns are only slightly sensitive to the degradation of bearings, with a reduction of their fragility for higher PGA values (Fig. 21a, orange curve), while these are highly sensitive to their own deterioration (Fig. 21a, green curve). This behavior of the columns fragility under bearing corrosion (Fig. 21a, orange curve) is explained by the nonlinear interaction between components under uneven corrosion patterns. At low IMs, the degraded bearings are not expected to yield, and the system behaves similarly to the as-built configuration, with a sligth column fragility increase due to the increased coefficient of friction of HTEBs. However, at higher IM levels, the corroded bearings, particularly HTFB and LTFB, undergo early yielding if corroded. In such conditions, the superstructure mass is practically decoupled from the columns. As a result, the displacement demand on the columns is expected to reduce, leading to a lower probability of exceeding the damage states. This explains the intersection between the orange and blue curves observed in Fig. 21a. Conversely, HTEBs are not significantly influenced by the corrosion of columns alone (Fig. 21b, green curve), and do only mildly so due to their own corrosion (Fig. 21b, orange curve). At the system level, the components' behaviors translate into an increase in fragility, which varies according to the deterioration scenario: the system is affected more by corrosion in bearings for PGA < 0.6, and more by the corrosion of columns for PGA > 0.6 (Fig. 21c, orange and green curves). These findings highlight that both components play a role in determining the system's fragility and that a retrofit intervention on just one of these would not result in substantial improvements in the safety of the bridge.

Secondly, with the proposed framework, we provide corrosion damage state-dependent fragilities for bridges, thereby being able to cover the full spectrum of uneven deterioration scenarios rather than limiting predictions to specific time points along the structure's lifespan. Our approach provides a complete map of seismic fragility across all deterioration scenarios, enabling quantification of the long-term effect of specific intervention actions (e.g. replacing a bearing, or repairing a column).. Moreover, embedding CDSs to SDSs probabilistic dependencies in a DBN allows coupling with driven fragility updating based on new data about deterioration (e.g. from inspections).

In conclusion, the capability to distill complex high-level system patterns to low-level component behaviors can inform better intervention planning, thus permitting better allocation of maintenance resources with a focus on the most deterioration-sensitive components or the most vulnerable ones. Nevertheless, the problem of managing these structures under seismic hazard remains challenging and problem-specific given the numerous uncertainties that govern both the deterioration and seismic phenomena, peculiar effects that can be triggered by corrosion at the component level during the seismic response, and the intricacies of the long-term decision-making problem. In this regard, the novel contribution of this work lies not only in providing a framework for fragility assessment under deterioration, but also in establishing a

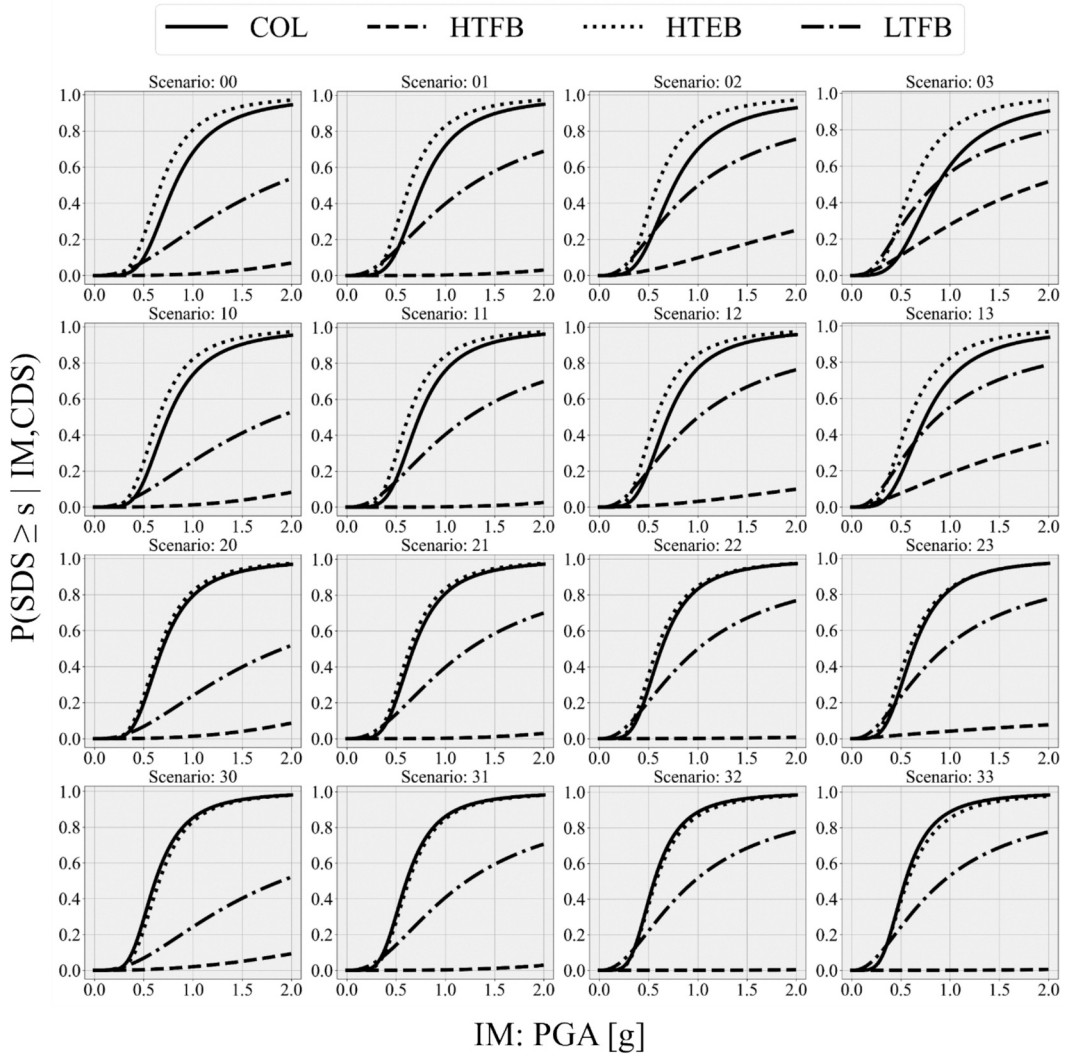

Fig. 18. State-dependent fragilities for the Complete SDS of the case study components according to 16 scenarios. Scenario ij: i = CDS_{COL}, j = CDS_{BEA}.

formulation consistent with advanced algorithmic decision-making tools. By explicitly quantifying deterioration transitions and state-dependent fragilities under heterogenous multi-component assumptions, the proposed methodology offers essential probabilistic inputs for data-driven infrastructure management under uncertainty. A first application of the framework in the context of algorithmic decision-making is presented in Metwally et al. [32], where the deterioration transitions derived from this methodology are adopted and integrated within partially observable Markov decision processes and deep reinforcement learning.

6. Conclusions

The study develops a dynamic Bayesian network (DBN) formulation for the evaluation of life-cycle seismic fragility of aging bridges subject to corrosion deterioration. Considering the bridge as a multi-component system, the methodology defines transitions between Corrosion Deterioration States (CDS), and Seismic Damage States (SDS) conditioned on CDSs and Intensity Measures (IM), for the structural components that are particularly vulnerable to both corrosion phenomena and seismic action, namely the columns and the bearings. The method allows for a structured probabilistic representation of damage and deterioration dynamics of the system in time, which is further reflected in a neat breakdown of the underlying DBN learning task into two distinct sub-tasks: (i) the estimation of non-stationary (time-variant) Markovian transitions describing the CDS evolution; and (ii) the determination of time-invariant state-dependent fragility curves regarding the SDS probabilities given IM and CDSs. Non-stationary Markovian transitions among CDS of the structural components are estimated through Monte Carlo simulation and based on available probabilistic models for corrosion initiation and propagation coupled with Gamma processes transitional uncertainties. The seismic fragility with respect to five states of seismic damage is learned through multinomial logistic regression based on the results of nonlinear dynamic analyses, in which uncertainties in materials, geometry, modeling, seismic action and corrosion process are accounted for.

The presented network is applied to a 4-span bridge, characterized by features common to aged bridges vulnerable to seismic events, i.e., poor detailing of the columns, presence of steel bearings, and Gerber joints. The DBN of this bridge is fitted under two distinct environmental conditions to further assess the significance of this factor. The analysis provides the transitions between CDS for the case-study bridge, highlighting that these enable the efficient probabilistic quantification of corrosion deterioration states for structural components and their combinations (i.e., deterioration scenarios) over the structural life-cycle. Time-invariant and state-dependent fragilities for the case study are also provided showcasing the sensitivity of seismic responses to corrosion scenarios. The life-cycle system fragility results show that splash

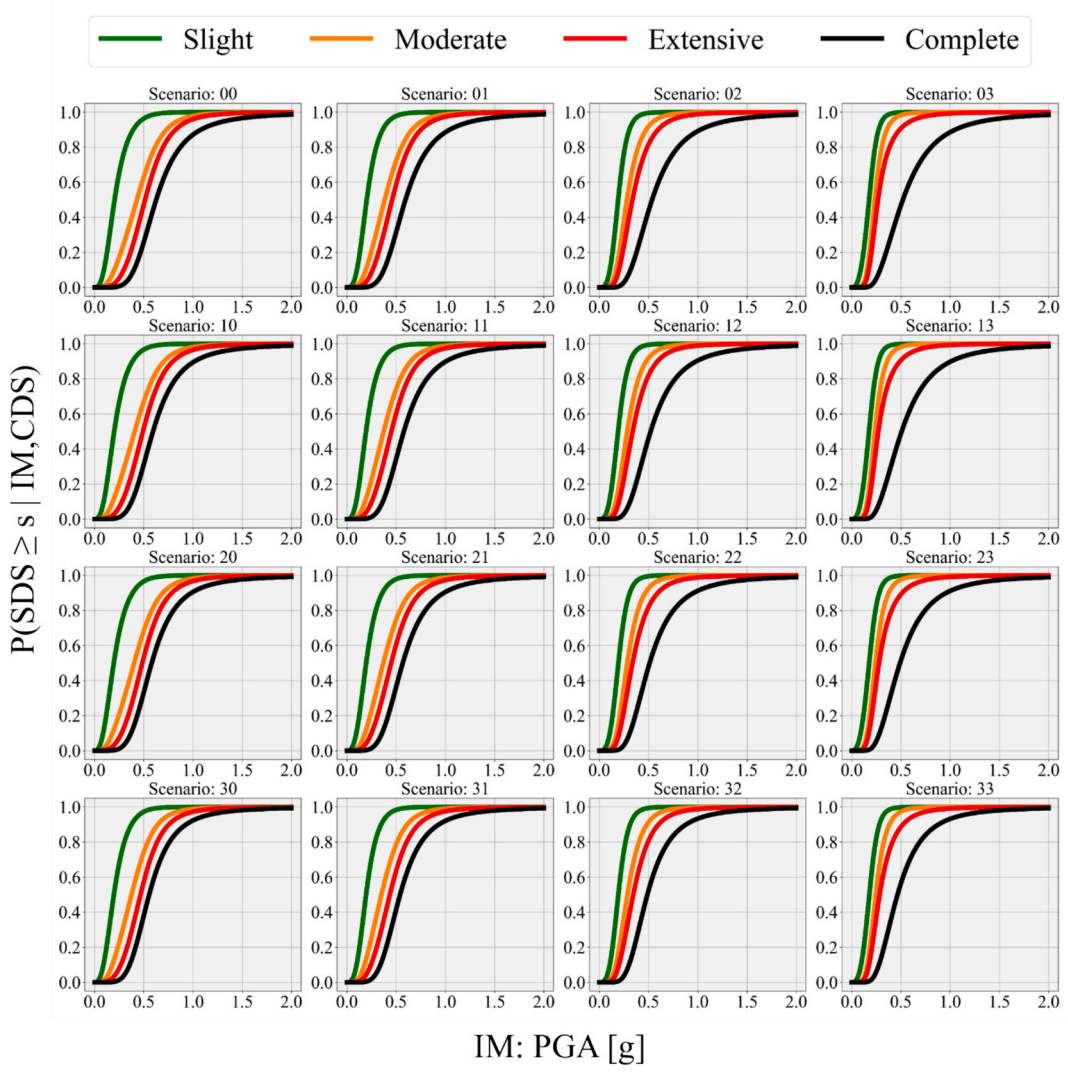

Fig. 19. State-dependent fragilities across the four SDS of the case study system according to 16 scenarios. Scenario ij: i = CDS_{COL}, j = CDS_{BEA}.

conditions can profoundly impact structural safety, particularly when corrosion affects the COL and HTEB components in this bridge archetype. COL were found to be the most sensitive to corrosion effects, while HTEB and COL were identified as the most valuable components from a system standpoint, thereby significantly affecting the system fragility across the 16 deterioration scenarios. Overall, the multi-component approach demonstrated significant potential in effectively identifying the most at-risk components within the system encompassing various corrosion scenarios. Furthermore, it offers a thorough assessment of the components' hierarchy of strengths, which is important for planning localized inspection and strengthening strategies.

Beyond fragility assessment for deteriorating RC bridges, the proposed DBN approach and the outcomes of the application serve as a basis to apply and further develop data-driven algorithmic decision making. Its capability to be extended, enabling adaptive fragility functions to on-site monitoring and/or inspections through additional observational nodes and inference on the probabilistic graphs has been discussed. Importantly, bringing the problem into a DBN form, makes it amenable to coupling with advanced decision-support systems relying on Markov decision processes, which have been shown to significantly improve large-scale infrastructure management in recent studies.

The scope of this work is to advance existing research on fragility analysis for RC bridges modelled as multi-component systems by: (i) discretizing corrosion into CDSs and coupling time-invariant, state-dependent fragilities, thus mapping seismic vulnerability across several deterioration scenarios; and (ii) revealing how columns and three bearing types interact under uneven corrosion scenarios, thereby guiding targeted interventions. While state-dependent fragilities are widely used in seismic risk modelling, this paper is the first to condition them on explicit, discrete corrosion states for multiple bridge components. Moreover, existing studies that model deterioration processes through DBNs do not consider seismic fragility for bridges and, therefore, lack component-specific corrosion transitions and state-dependent fragilities. Finally, beyond methodology, we provide a complete numerical demonstration with 16 deterioration scenarios, four structural components, and four seismic damage states, offering a benchmark for future research and calibration.

Along these lines, future research will delve into the integration of action and observation nodes within the probabilistic graph, thereby conceptualizing the management of life-cycle seismic safety for deteriorating RC bridges as a partially observable Markov decision process. This approach will facilitate the investigation of near-optimal inspection and maintenance strategies through deep reinforcement learning, aiming to strike an optimal balance between structural safety, maintenance costs, and environmental sustainability. To further support practical implementation, future work should also focus on a more detailed and data-informed quantification of life-cycle costs and benefits associated with intervention strategies. Towards this, Metwally et al. [32] adopts

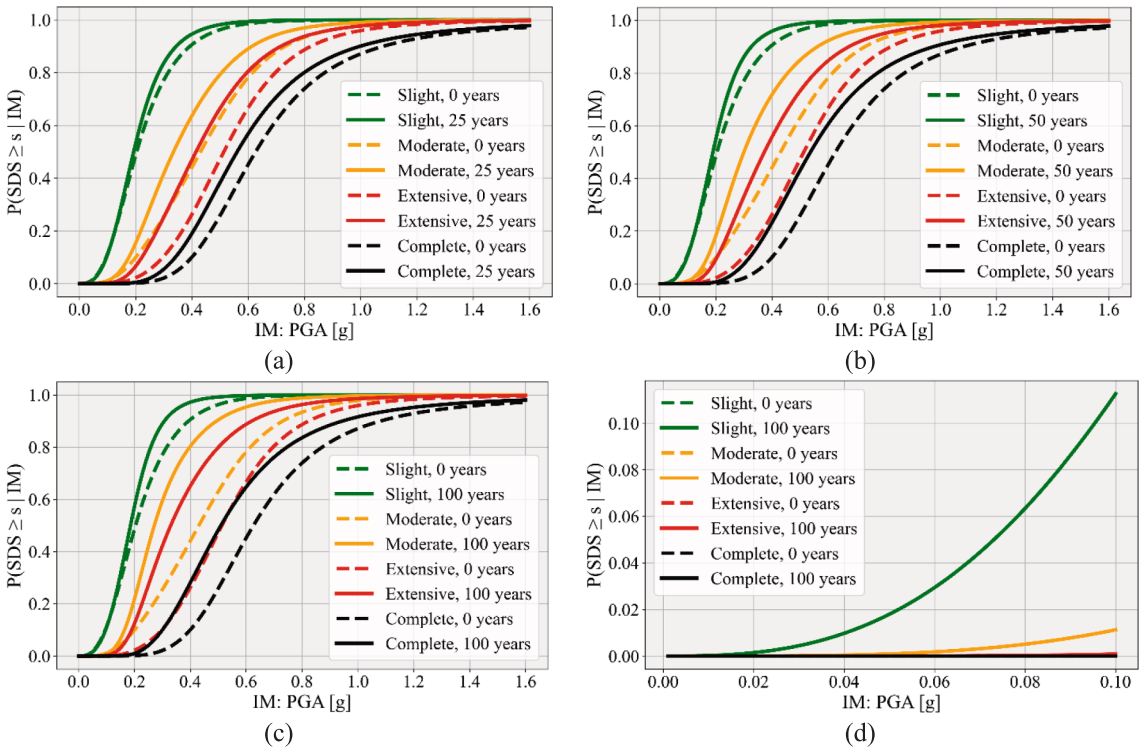

Fig. 20. System fragilities over the life-cycle of the case study bridge under different environmental conditions. a) Splash – 25 years; b) Splash – 50 years; c) Splash – 100 years; d) Atmospheric – 100 years.

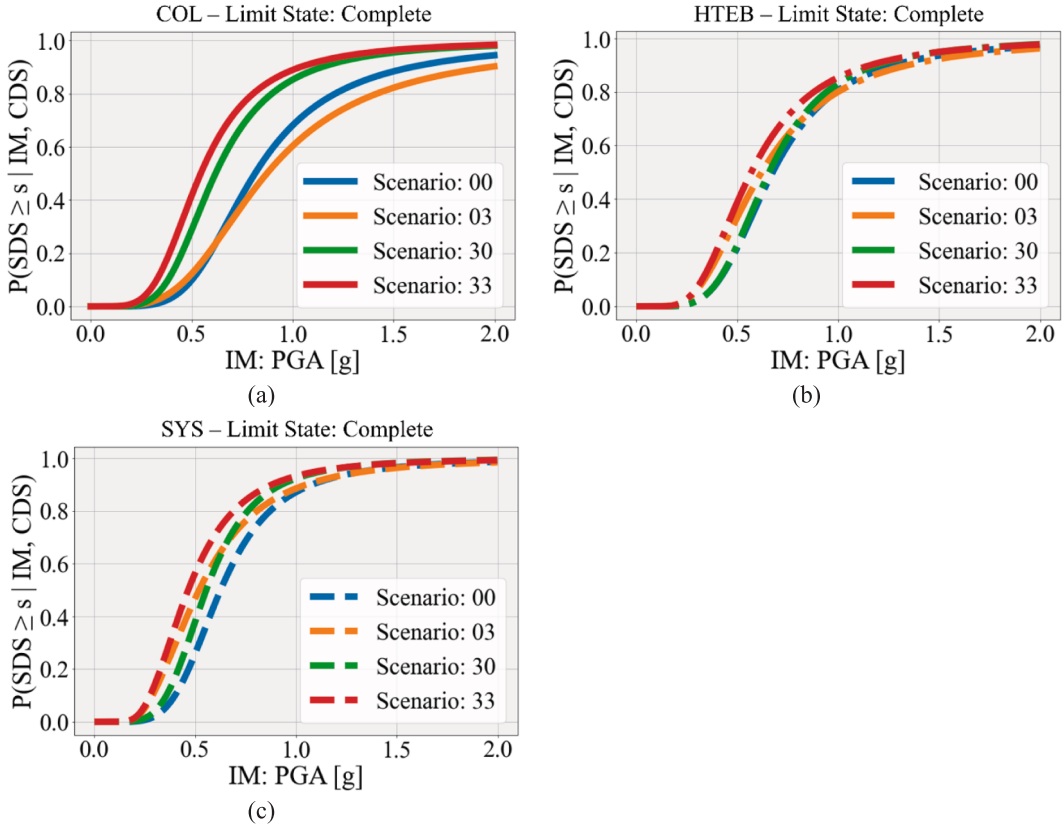

Fig. 21. Effects of specific corrosion scenarios on the seismic fragility of critical components and the system. a) COL components; b) HTEB components; c) System.

cost models for maintenance, retrofit, and replacement derived from literature, also extending the problem to a simplified two-bridge network to demonstrate the scalability of the method. Finally, extending the application of the proposed framework to larger infrastructure networks and to additional stressors, such as flooding or traffic loads, and including less seismic-prone components, such as decks and beams, it will become possible to conduct more comprehensive risk-based asset management, also at the regional scale.

CRediT authorship contribution statement

Filippo Molaioni: Writing – original draft, Methodology, Conceptualization, Writing – review & editing, Visualization, Formal analysis. **Charalampos P. Andriotis:** Writing – review & editing, Supervision, Conceptualization, Writing – original draft, Methodology. **Zila Rinaldi:** Supervision, Writing – review & editing, Conceptualization.

Declaration of competing interest

The authors declare that they have no known competing financial interests or personal relationships that could have appeared to influence the work reported in this paper.

Acknowledgments

Dr Molaioni would like to acknowledge the Erasmus + programme and Professor Alberto Meda. Dr. Andriotis would further like to acknowledge the support of the TU Delft AI Labs programme.

Appendix A

In this appendix, we present tables of β_0, the intercept, and β_1, the coefficient, for the multinomial logistic regression of SDSs in the logarithmic space of IM, i.e., the PGA of the seismic action, depending on the corrosion scenarios. These, denoted by a two-digit code, are based on the combination of CDSs for the COL and BEA components. These tables facilitate the calculation of the state-dependent fragility functions by applying Eq. (17) through the sum of the SoftMax functions of the corresponding SDS.

Table A1
Coefficients of the multinomial logistic regression. SDS: Slight.

SDS: Slight

			COL		HTFB		HTEB		LTFB		SYSTEM	
Scenario name	**CDS_{COL}**	**CDS_{BEA}**	**β_0**	**β_1**	**β_0**	**β_1**	**β_0**	**β_1**	**β_0**	**β_1**	**β_0**	**β_1**
00	**0**	**0**	−0.833	−0.641	1.181	−0.719	−0.180	−1.322	0.498	−0.383	−0.199	−1.341
01	**0**	**1**	−0.877	−0.569	2.889	−1.438	−0.286	−1.321	0.039	−0.368	−0.357	−1.322
02	**0**	**2**	−0.719	−0.351	1.430	−0.282	−0.602	−1.364	−0.361	−0.138	−1.261	−1.576
03	**0**	**3**	−0.678	−0.427	−0.045	−0.132	−1.090	−1.572	−1.442	−0.186	−2.835	−2.368
10	**1**	**0**	−1.057	−0.826	−0.028	−0.003	−0.184	−1.220	0.532	−0.414	−0.219	−1.231
11	**1**	**1**	−0.916	−0.659	2.427	−1.289	−0.307	−1.309	0.029	−0.377	−0.430	−1.336
12	**1**	**2**	−0.917	−0.549	1.871	−0.485	−0.701	−1.425	−0.556	−0.174	−1.353	−1.632
13	**1**	**3**	−0.791	−0.473	0.160	−0.077	−1.109	−1.554	−1.586	−0.201	−2.754	−2.338
20	**2**	**0**	−1.138	−1.001	−1.483	0.534	−0.233	−1.304	0.595	−0.473	−0.287	−1.260
21	**2**	**1**	−1.031	−0.799	1.208	−1.148	−0.271	−1.301	0.027	−0.411	−0.420	−1.289
22	**2**	**2**	−1.052	−0.655	1.980	−0.359	−0.613	−1.386	−0.849	−0.308	−1.456	−1.720
23	**2**	**3**	−1.013	−0.653	0.472	0.037	−1.105	−1.565	−1.773	−0.150	−2.505	−2.178
30	**3**	**0**	−0.863	−0.946	−1.769	0.844	−0.245	−1.369	0.626	−0.465	−0.523	−1.368
31	**3**	**1**	−0.853	−0.809	−1.523	0.781	−0.255	−1.295	0.057	−0.417	−0.511	−1.282
32	**3**	**2**	−0.915	−0.726	1.338	−1.256	−0.563	−1.361	−0.891	−0.367	−1.183	−1.487
33	**3**	**3**	−0.932	−0.688	1.154	−0.486	−1.033	−1.554	−1.801	−0.266	−2.334	−2.078

Table A2
Coefficients of the multinomial logistic regression. SDS: Moderate.

SDS: Moderate

			COL		HTFB		HTEB		LTFB		SYSTEM	
Scenario name	**CDS_{COL}**	**CDS_{BEA}**	**β_0**	**β_1**	**β_0**	**β_1**	**β_0**	**β_1**	**β_0**	**β_1**	**β_0**	**β_1**
00	**0**	**0**	−0.276	0.124	−3.249	1.580	−0.262	−0.354	−1.046	0.120	−0.291	−0.394
01	**0**	**1**	−0.397	0.089	−3.546	1.869	−0.290	−0.300	−1.197	−0.145	−0.270	−0.289
02	**0**	**2**	−0.455	0.101	−3.150	1.011	0.097	0.093	−0.821	−0.245	0.272	0.222
03	**0**	**3**	−0.470	0.038	−1.547	−0.255	0.587	0.293	−0.725	−0.246	0.823	0.626
10	**1**	**0**	−0.220	0.158	−2.726	1.129	−0.274	−0.360	−1.070	0.103	−0.315	−0.404
11	**1**	**1**	−0.361	0.052	−2.614	0.886	−0.302	−0.292	−1.202	−0.153	−0.186	−0.218
12	**1**	**2**	−0.387	0.040	−3.385	1.425	0.081	0.097	−0.895	−0.297	0.156	0.147
13	**1**	**3**	−0.416	0.023	−1.490	−0.130	0.606	0.309	−0.886	−0.277	0.828	0.618
20	**2**	**0**	−0.238	0.032	−2.540	0.871	−0.320	−0.384	−1.029	0.153	−0.308	−0.381
21	**2**	**1**	−0.331	−0.011	−3.412	1.757	−0.275	−0.289	−1.213	−0.146	−0.121	−0.146
22	**2**	**2**	−0.361	−0.018	−2.494	0.870	0.141	0.119	−0.968	−0.323	0.461	0.400
23	**2**	**3**	−0.405	−0.065	−1.052	0.056	0.548	0.283	−0.968	−0.350	0.794	0.640
30	**3**	**0**	−0.155	−0.051	−1.710	0.494	−0.284	−0.381	−1.085	0.268	−0.032	−0.206
31	**3**	**1**	−0.258	−0.085	−2.541	1.235	−0.264	−0.301	−1.230	−0.137	0.082	−0.041
32	**3**	**2**	−0.331	−0.048	−2.785	1.395	0.071	0.060	−1.028	−0.322	0.310	0.276
33	**3**	**3**	−0.342	−0.094	−0.394	−0.484	0.535	0.305	−1.019	−0.323	0.859	0.695

Table A3
Coefficients of the multinomial logistic regression. SDS: Extensive.

SDS: Extensive

			COL		HTFB		HTEB		LTFB		SYSTEM	
Scenario name	**CDS_{COL}**	**CDS_{BEA}**	**β_0**	**β_1**	**β_0**	**β_1**	**β_0**	**β_1**	**β_0**	**β_1**	**β_0**	**β_1**
00	**0**	**0**	−0.076	0.645	−2.768	1.388	1.247	1.462	−0.124	0.299	1.243	1.384
01	**0**	**1**	−0.198	0.585	−2.953	1.226	1.533	1.533	0.139	0.285	1.591	1.400
02	**0**	**2**	−0.348	0.458	−0.551	−0.065	2.150	1.683	0.615	0.292	2.545	1.612
03	**0**	**3**	−0.369	0.432	0.273	0.220	2.611	1.735	1.197	0.411	3.485	1.928
10	**1**	**0**	0.072	0.701	−2.671	1.043	1.158	1.356	−0.129	0.334	1.129	1.242
11	**1**	**1**	−0.136	0.547	−3.523	1.845	1.446	1.441	0.100	0.266	1.475	1.283
12	**1**	**2**	−0.178	0.479	−0.878	0.100	2.104	1.645	0.562	0.237	2.408	1.549
13	**1**	**3**	−0.220	0.440	0.211	0.245	2.601	1.723	1.057	0.299	3.433	1.921
20	**2**	**0**	0.147	0.727	−2.042	0.830	1.136	1.345	−0.164	0.418	1.033	1.152
21	**2**	**1**	−0.023	0.532	−3.151	1.644	1.377	1.378	0.089	0.264	1.346	1.196
22	**2**	**2**	−0.063	0.431	−1.199	−0.090	2.082	1.631	0.514	0.199	2.427	1.578
23	**2**	**3**	−0.083	0.418	0.005	0.229	2.492	1.676	0.967	0.160	3.018	1.684
30	**3**	**0**	0.235	0.781	−0.905	0.394	1.093	1.360	−0.203	0.401	1.040	1.144
31	**3**	**1**	0.042	0.576	−1.798	0.945	1.325	1.386	0.062	0.285	1.310	1.193
32	**3**	**2**	−0.016	0.511	−2.994	1.968	1.917	1.563	0.489	0.213	2.043	1.350
33	**3**	**3**	0.034	0.518	−0.711	−0.171	2.404	1.666	0.913	0.173	2.782	1.583

Table A4
Coefficients of the multinomial logistic regression. SDS: Complete.

SDS: Complete

			COL		HTFB		HTEB		LTFB		SYSTEM	
Scenario name	**CDS_{COL}**	**CDS_{BEA}**	**β_0**	**β_1**	**β_0**	**β_1**	**β_0**	**β_1**	**β_0**	**β_1**	**β_0**	**β_1**
00	**0**	**0**	1.747	2.952	0.056	0.495	3.052	4.034	0.372	1.373	3.530	4.408
01	**0**	**1**	1.886	2.756	−1.090	1.104	3.399	4.155	0.879	1.456	3.894	4.510
02	**0**	**2**	1.793	2.232	0.275	0.782	3.968	4.212	1.240	1.621	4.772	4.626
03	**0**	**3**	1.473	2.203	0.574	1.129	4.145	4.270	1.764	1.738	5.598	4.886
10	**1**	**0**	2.005	2.985	0.526	0.368	3.094	3.892	0.376	1.329	3.666	4.308
11	**1**	**1**	2.060	2.916	−1.277	1.312	3.414	4.070	0.899	1.461	3.937	4.434
12	**1**	**2**	2.106	2.628	−0.332	0.623	4.007	4.205	1.228	1.587	4.774	4.603
13	**1**	**3**	1.832	2.403	0.179	0.932	4.284	4.293	1.667	1.593	5.671	4.933
20	**2**	**0**	2.303	3.127	0.887	0.294	3.059	3.938	0.313	1.381	3.720	4.291
21	**2**	**1**	2.332	3.029	−0.269	0.641	3.341	4.103	0.884	1.486	3.939	4.350
22	**2**	**2**	2.461	2.838	−2.321	1.070	3.998	4.271	1.257	1.525	4.914	4.673
23	**2**	**3**	2.410	2.727	−1.050	0.519	4.268	4.295	1.581	1.483	5.453	4.747
30	**3**	**0**	2.741	3.376	0.258	0.328	3.111	4.084	0.343	1.351	3.967	4.394
31	**3**	**1**	2.715	3.202	−0.003	0.217	3.388	4.132	0.915	1.475	4.139	4.355
32	**3**	**2**	2.900	3.046	−2.149	1.234	3.997	4.277	1.324	1.511	4.877	4.560
33	**3**	**3**	2.924	2.972	−3.898	2.517	4.341	4.348	1.602	1.450	5.543	4.759

Appendix B

This Appendix is intended to zoom into the details of the interdependent structural behavior of the bridge components. We look into specific deterioration scenarios, representative of non-uniform deterioration in the structural system, and the mutual mechanical interaction of structural components under these circumstances. The primary goal is to highlight how the proposed method efficiently captures complex structural hierarchy of strength/fragility of the different system components, and its changes with the onset of uneven corrosion. For this, we needed a more balanced hierarchy of strengths in the as-built condition; therefore, the original strength of HTFB, which resulted largely safe in the above presented structural analysis, has been weakened by a factor of 2. Furthermore, to better decipher behavioral interplay among components, results are presented by isolating the bridge transversal and longitudinal behavior.

The first case to be examined concerns the transverse behavior of the COL-HTFB subsystem. It is seen in the analysis of the fragility curves for these components regarding the transverse direction that corrosion of COL components positively affects the fragility of BEA components, thus decreasing it. This effect is specifically highlighted for the HTFB in Fig. B1, where fragilities in the transversal direction are presented for corrosion scenarios 10: Initial for COL, Sound for BEA; 20: Progressive for COL, Sound for BEA; and 30: Critical for COL, Sound for BEA. These are compared with the as-built scenario, i.e. 00.

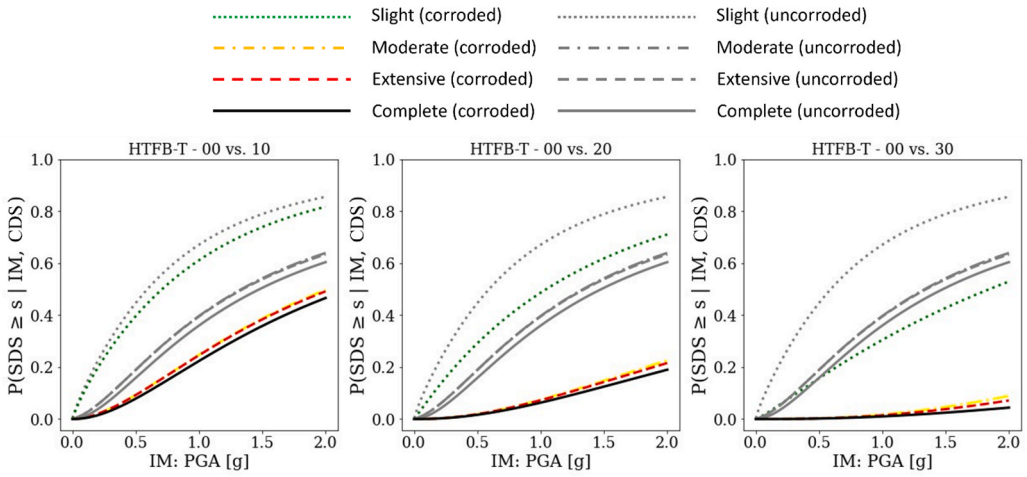

Fig. B1. Fragilities of HTFB in the transverse direction. a) scenario 00 vs. 10; b) scenario 00 vs. 20; c) scenario 00 vs. 30.

This effect can be attributed to the fact that, since the columns are directly connected to the ground, and, at the same time, they support the deck and the HTFB devices, their premature failure triggered by corrosion could prevent greater transverse relative displacement between the deck and the top of the pier. This displacement is used as the engineering demand parameter adopted for BEA components. According to this effect, in Fig. B2, illustrative sketches of the global mechanisms that can occur in a COL-HTFB subsystem (Fig. B2a) are presented. In the case of sound structure or uniform widespread corrosion, it is impossible to clearly guess a specific mechanism, and therefore, a mixed sidesway mechanism is assumed (Fig. B2c), with plasticity (i.e., gray hinges or rollers) widespread both on the support components and the columns. In the case of localized corrosion in the columns, it is reasonable to expect that they may undergo premature plasticization, thus resulting in a column sidesway mechanism (Fig. B2d), which acts as an isolator for the forces to which the bearings are subjected during the plastic dynamic behavior.

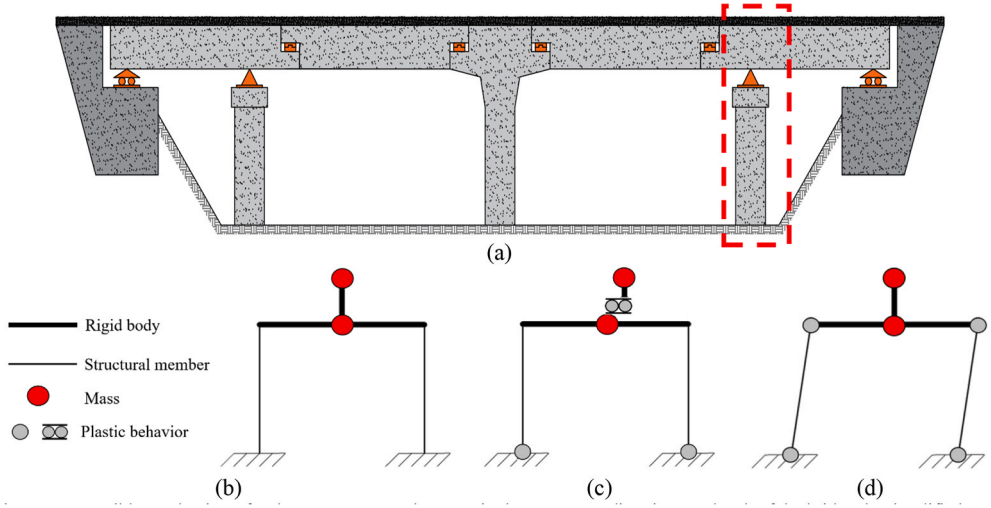

Fig. B2. Possible mechanisms for the COL-HTFB subsystem in the transverse direction. a) sketch of the bridge; b) simplified model of the transversal COL-HTFB subsystem; c) mixed sidesway mechanism; d) column sidesway mechanism.

This effect is further highlighted by showing the nonlinear behavior of critical components during a ground motion with respect to the corrosion scenarios 00 and 30 (i.e., sound structure and critical corrosion in COL components only, respectively). The comparison reported in Fig. B3 is made by analyzing the displacement and curvature ductility time histories of column components, and the force–displacement cyclic behavior of the BEA components.

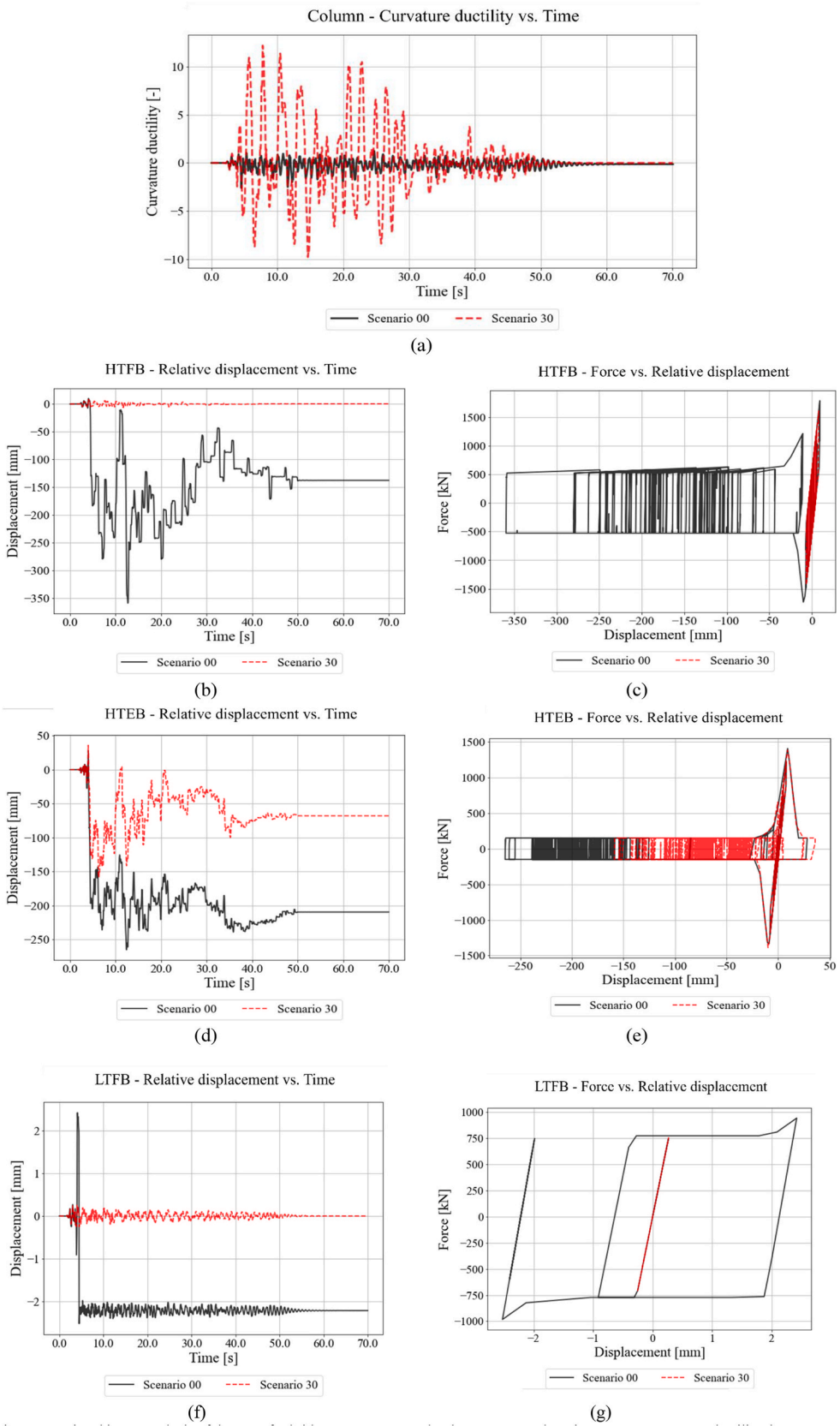

Fig. B3. Time history analysis of the EDP for bridge components under the same ground motion. a) COL curvature ductility; b) HTFB relative displacements; c) HTFB force vs. relative displacement; d) HTEB relative displacements; e) HTEB force vs. relative displacement; f) LTFB relative displacements; g) LTFB force vs. relative displacement.

The notable feature here is that the bridge components exhibit totally different structural behaviors for corrosion scenarios 00 and 30 under the same ground motion. In the 00 scenario, both COL and the three BEA components enter the plastic regime: the former reaches curvature ductility up to 2 (Fig. B3a, black curve), while the latter shows maximum displacements in the order of 350 mm, 350 mm and 2 mm, and residual displacement of around 150 mm, 200 mm and 2 mm, for HTFB, HTEB and LTFB, respectively (Fig. B3b,d,f, black curves). Conversely, for the 30 scenario where the COL reaches excessive curvature ductility up to 12 (Fig. B3a, red curve), the dissipative demand on bearing components almost vanishes, with HTFB and LTFB displaying largely elastic behavior (Fig. B3c,g, red curves), and HTEB reducing its maximum displacement to l50mm and its residual displacement to less than 70 mm (Fig. B3d, red curve). This illustrates how non-uniform corrosion among components can result in significant changes in their strength hierarchy and the displayed cyclic behavior patterns, which in turn reflects on the global damage mechanisms and, ultimately, the structural fragility.

At the longitudinal direction, the whole system is more complex, due to the large number of components and masses involved during a mechanism and the mutual interaction involving all of these during the seismic shaking. Such dynamic effects in the nonlinear regime do not allow for such clear identification changes in the global behavior due to the substantial changes in the hierarchies of strength caused by non-uniform corrosion scenarios on the structure. Having corroded columns only, depending on the dynamic characteristics of the seismic action, could lead to differential plastic behaviors in the bearing components. Consequently, the mechanism, even following uneven corrosion phenomena, always remains one of mixed type, as shown in the sketches in Fig. B4. Furthermore, it turns out that, in the longitudinal direction, the BEA components are not very sensitive to corrosion in the columns, as evidenced by the fragility curves shown in Fig. B5.

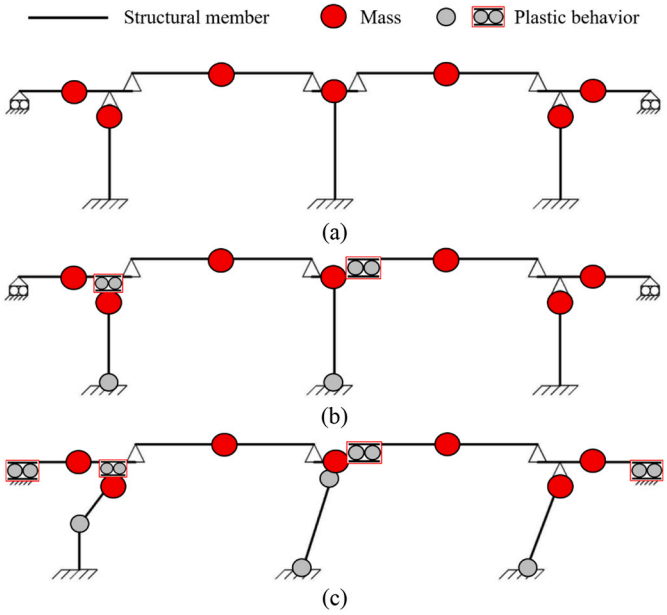

Fig. B4. Possible mechanisms in the longitudinal direction. a) simplified sketch of the bridge; b) a mixed mechanism without corrosion; b) a mixed mechanism with corrosion in columns only.

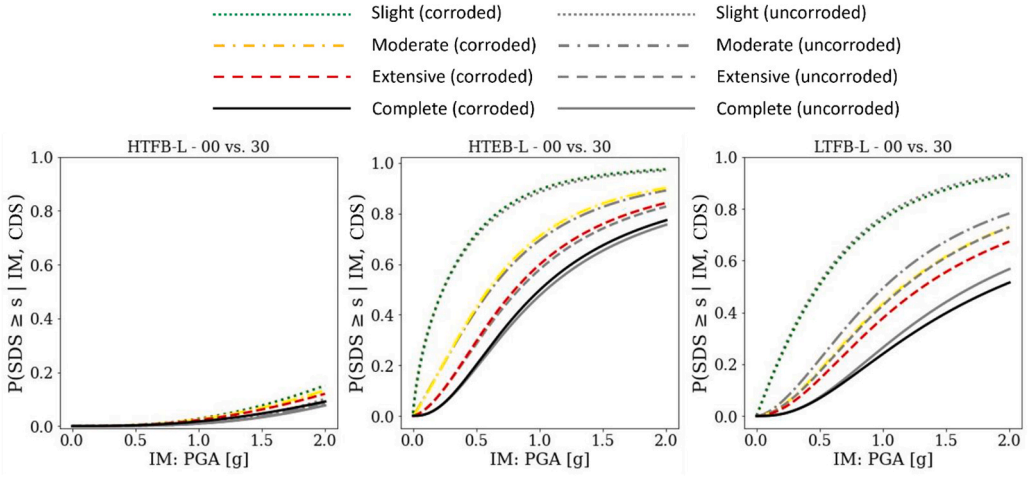

Fig. B5. Fragilities of BEA components in the longitudinal direction. a) HTFB scenario 00 vs. 30; b) HTEB scenario 00 vs. 30; c) LTFB scenario 00 vs. 30.

Overall, based on the structural behavior features highlighted throughout Appendix B, it can be concluded that the impact of corrosion on structural fragility manifests in local and global mechanism changes. Notably, BEA components are protected through the column sidesway

mechanism in the transverse direction. On the other hand, longitudinal direction complexities are exacerbated by mass distribution and non-linearities, resulting in a non-sensitive behavior of the HTFB and HTEB components in the presence of columns' corrosion. Finally, considering unexpected corrosion scenarios during the structural life-cycle, the presented findings underline that the proposed DBN approach is suitable to account for the resulting changes in inelastic behaviors. In this way, it offers a valuable computational means for capturing and simulating evolving failure mechanisms and, therefore, for understanding how intervention and monitoring decisions have to be planned, prioritized, and updated in time.

Data availability

No data was used for the research described in the article.

References

[1] Ali SM, Khan AN, Rahman SMH, Reinhorn AM. A Survey of Damages to Bridges in Pakistan after the Major Earthquake of 8 October 2005. Earthq Spectra 2011;27:947–70.

[2] Alipour A, Shafei B, Shinozuka M. Performance Evaluation of Deteriorating Highway Bridges located in High Seismic areas. J Bridg Eng 2011;16:597–611.

[3] Andriotis CP, Papakonstantinou K. Extended and Generalized Fragility Functions. J Eng Mech 2018.

[4] Andriotis CP, Papakonstantinou K. Managing engineering systems with large state and action spaces through deep reinforcement learning. *ArXiv*, *abs/1811.0*.

[5] Banerjee S, Chi C. State-dependent fragility curves of bridges based on vibration measurements. Probab Eng Mech 2013;33:116–25.

[6] Bertolini L, Elsener B, Redaelli E, Polder RB. *Corrosion of Steel in Concrete: Prevention*. Repair: Diagnosis; 2004.

[7] Biondini F, Camnasio E, Palermo A. Lifetime seismic performance of concrete bridges exposed to corrosion. Struct Infrastruct Eng 2014;10:880–900.

[8] Biondini, F., Camnasio, E., & Titi, A. (2015). *Seismic resilience of concrete structures under corrosion. July*, 2445–2466. doi:10.1002/eqe.

[9] Biondini F, Frangopol DM. Life-cycle performance of deteriorating structural systems under uncertainty. Review Journal of Structural Engineering-Asce 2016;142.

[10] Castel A, François R, Arliguie G. Mechanical behaviour of corroded reinforced co–crete beams - Part 1: experimental study of corroded beams. Materials and Structures/Materiaux et Constructions 2000;33(233):539–44.

[11] Castel A, François R, Arliguie G. Mechanical behaviour of corroded reinforced concrete beams—Part 2: Bond and notch effects. Mater Struct 2000;33:545–51.

[12] Choe D, Gardoni P, Rosowsky D, Haukaas T. Probabilistic capacity models and seismic fragility estimates for RC columns subject to corrosion 2008;93:383–93. https://doi.org/10.1016/j.ress.2006.12.015.

[13] Choi, E. (2002). *Seismic analysis and retrofit of mid-America bridges*.

[14] Choine MN, Kashani MM, Lo'es, L. N., O'Connor, A., Crewe, A. J., Alexander, N. A., & Padgett, J. E.. Nonlinear dynamic analysis and seismic fragility assessment of a corrosion damaged integral bridge. International Journal of Structural Integrity 2016;7:227–39.

[15] Coccia S, Imperatore S, Rinaldi Z. Influence of corrosion on the bond strength of steel rebars in concrete. Materials and Structures/Materiaux et Constructions 2016;49(1–2):537–51. https://doi.org/10.1617/s11527-014-0518-x.

[16] Coronelli D, Gambarova P. Structural Assessment of Corroded Reinforced Concrete Beams: Modeling guidelines. J Struct Eng 2004. https://doi.org/10.1061/(asce)0733-9445(2004)130:8(1214).

[17] Cui F, Zhang H, Ghosn M, Xu Y. Seismic fragility analysis of deteriorating RC bridge substructures subject to marine chloride-induced corrosion. Eng Struct 2018;155:61–72.

[18] Di Di Carlo F, Meda A, Molaioni F, Rinaldi Z. Experimental evaluation of the corrosion influence on the structural response of Gerber half-joints. Eng Struct 2023.

[19] Di Carlo, F., Rinaldi, Z., Meda, A., & Molaioni, F. (2024). Experimental Behaviour of Prestressed Concrete Beams Under Simultaneous Sustained Loading and Corrosion. Submitted, *under review*.

[20] Siemes A, Edvardsen C. Duracrete: Service life design for concrete structures; 1999.

[21] Fema.hazus-mh mr1, Technical Manual, Federal Emergency Management Agency 2003 Washington, DC.

[22] Gentile R, Galasso C. Hysteretic energy-based state-dependent fragility for ground-motion sequences. Earthquake Engineering & Structural Dynamics 2021;50(4):1187–203.

[23] Ghosh J, Padgett JE. Aging Considerations in the Development of Time-Dependent Seismic Fragility Curves. Journal of Structural Engineering-Asce 2010;136:1497–511.

[24] Ghosh J, Padgett JE. Impact of multiple component deterioration and exposure conditions on seismic vulnerability of concrete bridges. Earthquakes Struct 2012;3:649–73.

[25] Hlaing N, Morato PG, Nielsen JS, Amirafshari P, Kolios AJ, Rigo P. Inspection and maintenance planning for offshore wind structural components: integrating fatigue failure criteria with Bayesian networks and Markov decision processes. Struct Infrastruct Eng 2022;18:983–1001.

[26] Imperatore S, Rinaldi Z, Drago C. Degradation relationships for the mechanical properties of corroded steel rebars. Constr Build Mater 2017;148:219–30. https://doi.org/10.1016/j.conbuildmat.2017.04.209.

[27] Kim S, Frangopol DM, Soliman M. Generalized Probabilistic Framework for Optimum Inspection and Maintenance Planning. Journal of Structural Engineering-Asce 2013;139:435–47.

[28] Kumar R, Gardoni P, Sánchez-Silva M. Effect of cumulative seismic damage and corrosion on the life-cycle cost of reinforced concrete bridges. Earthquake Engineering & Structural Dynamics 2009;38.

[29] Luque J, vStraub, D.. Risk-based optimal inspection strategies for structural systems using dynamic Bayesian networks. Struct Saf 2019.

[30] Mander, J. B., Kim, D., Chen, S. S., & Premus, G. J. (1996). *Response of Steel Bridge Bearings to Reversed Cyclic Loading by*.

[31] Mander J, Priestley MJ, Park R. Theoretical stress strain model for confined concrete. Journal of Structural Engineering-asce 1988;114:1804–26.

[32] Z. Metwally C.P. Andriotis F. Molaioni Managing aging bridges under seismic hazards through deep reinforcement learning 2024 Copenhagen.

[33] McKenna F. OpenSees: a Framework for Earthquake Engineering simulation. Comput Sci Eng 2011;13:58–66.

[34] Meda A, Mostosi S, Rinaldi Z, Riva P. Experimental evaluation of the corrosion influence on the cyclic behaviour of RC columns. Eng Struct 2014;153:264–78.

[35] Molaioni F, Pampanin S, Rinaldi Z. Simplified Methodology for the Evaluation of Corrosion Effects on Seismic risk of Reinforced Concrete Frame buildings. In: *2nd fib Symposium on Concrete and Concrete Structures*; 2021. p. 281–8.

[36] Molaioni, F., Rinaldi, Z., Andriotis, C. P. (2023). Assessing life-cycle seismic fragility of corroding reinforced concrete bridges through dynamic Bayesian networks. Proc. of the eighth Int. Sym. on Life-Cycle Civil Eng. (IALCCE. *2-6 July 2023*. Milan, Italy: Politecnico di Milano; 2023. p. 523–30.

[37] F. Molaioni C.P. Andriotis Z. Rinaldi A dynamic Bayesian network approach for multi-component fragility of aging bridges 2024 Copenhagen.

[38] Morato PG, Andriotis CP, Papakonstantinou K, Rigo P. Inference and dynamic decision-making for deteriorating systems with probabilistic dependencies through Bayesian networks and deep reinforcement learning. Reliab Eng Syst Saf 2022;235:109144.

[39] Morato, P. G., Papakonstantinou, K., Andriotis, C. P., Nielsen, J. S., & Rigo, P. (2020). Optimal Inspection and Maintenance Planning for Deteriorating Structures through Dynamic Bayesian Networks and Markov Decision Processes. ArXiv, abs/2009.0.

[40] Nardin C, Marelli S, Bursi OS, Sudret B, Broccardo M. UQ state-dependent framework for seismic fragility assessment of industrial components. Reliab Eng Syst Saf 2025:111067.

[41] Nielson BG, DesRoches R. Seismic fragility methodology for highway bridges using a component level approach. Earthquake Engineering & Structural Dynamics 2007;36.

[42] Orlacchio M, Baltzopoulos G, Iervolino I. Simplified state-dependent seismic fragility assessment. Earthquake Engineering & Structural Dynamics 2024;53(6):2099–121.

[43] Padgett J.E., DesRoches R. Bridge damage-functionality using expert opinion survey.8th National Conference on Earthquake Engineering, Earthquake Engineering Research Institute, San Francisco, 2006.

[44] Papakonstantinou K, Andriotis CP, Shinozuka M. POMDP and MOMDP solutions for structural life-cycle cost minimization under partial and mixed observability. Struct Infrastruct Eng 2018;14:869–82.

[45] Papakonstantinou KG, Shinozuka M. Probabilistic model for steel corrosion in reinforced concrete structures of large dimensions considering crack effects. Eng Struct 2013;57:306–26. https://doi.org/10.1016/j.engstruct.2013.06.038.

[46] Papakonstantinou K, Shinozuka M. Optimum inspection and maintenance policies for corroded structures using partially observable Markov decision processes and stochastic, physically based models. Probab Eng Mech 2014;37:93–108.

[47] Pedone L, Gentile R, Galasso C, Pampanin S. Energy-based procedures for seismic fragility analysis of mainshock-damaged buildings. Front Built Environ 2023;9:1183699.

[48] Priestley MJN, Seible F, Calvi GM. *Seismic Design and Retrofit* of Bridges. In Seismic Design and Retrofit of Bridges 1996. https://doi.org/10.1002/9780470172858.

[49] Ramirez, J. A., Frosch, R. J., Sozen, M., & Turk, A. M. (2000). *Handbook for the Post-Earthquake Safety Evaluation of Bridges and Roads*.

[50] Rinaldi Z, Di Di Carlo F, Spagnuolo S, Meda A. Influence of localised corrosion on the cyclic response of reinforced concrete columns. Eng Struct 2022.

[51] Rodriguez J, Ortega LM, Casal J. Load carrying capacity of concrete structures with corroded reinforcement. Constr Build Mater 1997. https://doi.org/10.1016/S0950-0618(97)00043-3.

[52] *fib Bulletin 34. Model Code for Service Life Design*. (2006).

[53] Shekhar S, Ghosh J. Improved Component-Level Deterioration Modeling and Capacity Estimation for Seismic Fragility Assessment of Highway Bridges 2021;7(4):1–23. https://doi.org/10.1061/AJRUA6.0001154.

[54] Shekhar S, Ghosh J, Padgett JE. Seismic life-cycle cost analysis of ageing highway bridges under chloride exposure conditions: modelling and recommendations. Struct Infrastruct Eng 2018;14:941–66.

[55] Shinozuka, M., Feng, M. Q., Kim, H. Y., Uzawa, T., & Ueda, T. (2000). *STATISTICAL ANALYSIS OF FRAGILITY CURVES*.

[56] Silano, L. G. (1993). *Bridge inspection and rehabilitation : a practical guide*.
[57] Song J, Kang WH. System reliability and sensitivity under statistical dependence by matrix-based system reliability method. Struct Saf 2009;31(2):148–56.
[58] Stewart MG, Al-Harthy A. Pitting corrosion and structural reliability of corroding RC structures : Experimental data and probabilistic analysis 2008;93:373–82. https://doi.org/10.1016/j.ress.2006.12.013.
[59] Stewart MG, Rosowsky DV. Time-dependent reliability of deteriorating reinforced concrete bridge decks. Struct Saf 1998;20:91–109.
[60] Tuutti, K. (1982). *Corrosion of steel in concrete*.
[61] Val DV, Melchers RE. RELIABILITY OF DETERIORATING RC SLAB BRIDGES. Journal of Structural Engineering-Asce 1997;123:1638–44.
[62] Vidal T, Castel A, Franc R. Analyzing crack width to predict corrosion in reinforced concrete 2004;34:165–74. https://doi.org/10.1016/S0008-8846(03)00246-1.
[63] Vlachos C, Papakonstantinou K, Deodatis G. Predictive model for site specific simulation of ground motions based on earthquake scenarios. Earthquake Engineering & Structural Dynamics 2018;47:195–218.
[64] Vlašić A, Srbić M, Skokandić D, Mandić IA. Post-Earthquake Rapid damage Assessment of Road Bridges in Glina County. Buildings 2022;12(1):42.
[65] Vu KAT, Stewart MG. Structural reliability of concrete bridges including improved chloride-induced corrosion models. Struct Saf 2000;22:313–33.
[66] Yashinsky, M., Moehle, J. P., & Eberhard, M. O. (2014). *Earthquake Damage to Bridges*.
[67] S. Yi K.G. Papakonstantinou C.P. Andriotis J. Song Appraisal and mathematical properties of fragility analysis methods In Proceedings of the 13th International Conference on Structural Safety and Reliability (ICOSSAR) 2022.
[68] Yuan W, Guo A, Li H. Seismic failure mode of coastal bridge piers considering the effects of corrosion-induced damage. Soil Dyn Earthq Eng 2017. https://doi.org/10.1016/j.soildyn.2016.12.002.